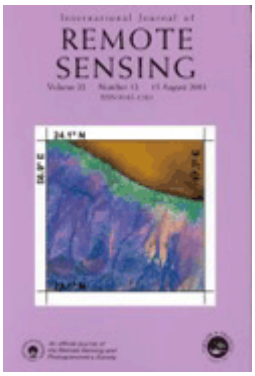

Assimilating synthetic GOES-R radiances in cloudy conditions using an ensemble-based method

Journal:	*International Journal of Remote Sensing*
Manuscript ID:	TRES-PAP-2009-0089
Manuscript Type:	Research Paper
Date Submitted by the Author:	10-Feb-2009
Complete List of Authors:	Zupanski, Dusanka; Colorado State University, CIRA Zupanski, Milija; Colorado State University, CIRA Grasso, Lewis; Colorado State University, CIRA Brummer, Renate; Colorado State University, CIRA Jankov, Isidora; Colorado State University, CIRA Lindsey, Daniel; NOAA/NESDIS/StAR, RAMMB Sengupta, Manajit; Colorado State University, CIRA DeMaria, Mark; NOAA/NESDIS/StAR, RAMMB
Keywords:	CLOUDS, INFRARED
Keywords (user defined):	DATA ASSIMILATION, INFORMATION MEASURES, GOES-R

Assimilating synthetic GOES-R radiances in cloudy conditions using an ensemble-based method

Dusanka Zupanski[1,*], Milija Zupanski[1], Lewis. D. Grasso[1], Renate Brummer[1], Isidora Jankov[1], Daniel Lindsey[2], Manajit Sengupta[1], and Mark DeMaria[2]

[1]Colorado State University/Cooperative Institute for Research in the Atmosphere, Fort Collins, Colorado, U.S.A.
[2]NOAA/NESDIS/StAR, Fort Collins, Colorado, U.S.A.

To be submitted to International Journal of Remote Sensing

Abstract

The Weather Research and Forecasting (WRF) model and the Maximum Likelihood Ensemble Filter (MLEF) data assimilation approach are used to examine the potential impact of observations from the future Geostationary Operational Environmental Satellite, generation R (GOES-R) on improving our knowledge about clouds. Synthetic radiances are assimilated from the 10.35 μm channel of the GOES-R Advanced Baseline Imager (ABI) employing a "non-identical twins" experimental setup. The experimental results are examined for an extratropical cyclone named Kyrill that produced unusually strong winds, widespread damage, and fatalities in Western Europe in January 2007. The data assimilation problem is especially challenging for this case, as there is a large error in the model-simulated radiances resulting from incorrect cloud location. Although this problem is difficult to eliminate the data assimilation results indicate the potential of GOES-R data to significantly reduce these errors.

[*]Corresponding author address: Dusanka Zupanski, Colorado State University, Cooperative Institute for Research in the Atmosphere, Foothill Campus, Fort Collins, CO 80523-1735, U.S.A. E-mail: Zupanski@cira.colostate.edu

1. Introduction

Current and new satellite missions provide a wealth of information to improve our understanding of weather, climate, ocean and the Earth system in general. This study is motivated by the needs of new satellite missions to undergo all necessary preparations well before the satellite launch in order to make sure that the observations will be successfully used as soon as they become available. Data assimilation studies, such as this one, are being employed to prepare methodologies capable of addressing the challenges of the new satellite missions. These methodologies should be able to effectively assimilate the new satellite observations and quantify the information content of the assimilated data. This study focuses on the data assimilation needs of the next-generation series of Geostationary Operational Environmental Satellite (GOES-R) mission, currently scheduled for launch in the year 2015. Our objective is to explore the information content and further improve capabilities of the current state-of-the-art data assimilation methods in order to extract maximum information from the GOES-R data, especially in cloudy scenes.

Data assimilation methods have been successfully used to assimilate various satellite observations in order to improve weather, climate, ocean, hydrological, and ecological forecasts over several decades (L'Ecuyer et al. 2006; Reichle 2007; Carton and Giese 2008; Hollingsworth et al. 2008; Jung et al. 2008; Keppenne et al. 2008; and Migliorini et al. 2008 are some recent examples). It is commonly accepted that satellite and other remote sensing observations are a major source of information for today's geophysical models due to wide spatial and high temporal coverage as compared to the non-remote sensing (the so-called conventional) observations. Current state-of-the-art data assimilation methods typically assimilate satellite radiances or brightness temperatures, rather than derived model state parameters (retrievals). This is mainly because the observation errors of the radiances/brightness temperatures are better known (and are typically less biased) than the observation errors of the retrievals.

One of the most difficult challenges of satellite data assimilation is assimilation of satellite radiances in cloudy conditions. Some of the major difficulties arise from the nonlinear and often discontinuous character of modeled cloud microphysical processes and from largely unknown forecast error covariances of these processes. Because of these and many other difficulties, the operational weather centers have been assimilating clear-sky (or cloud cleared) radiances for decades, thus discarding important information about clouds and precipitation, as well as other atmospheric variables, contained in the cloudy visible, infrared and microwave radiances (more about the importance of assimilation of cloudy radiances can be found, for example, in Andersson et al. 2005 and Errico et al. 2007). Nevertheless, cloudy satellite retrievals can also bring important information about precipitation and clouds, as demonstrated in the recent studies by Hou and Zhang (2007) and Lin et al. (2007), where the Tropical Rainfall Measuring Mission (TRMM) Microwave Imager (TMI) and Special Sensor Microwave Imager (SSM/I) tropical rainfall observations were assimilated.

Thanks to advancements in numerical modeling and data assimilation methods, assimilation of cloudy radiances has advanced significantly in the last decade, especially in the atmospheric data assimilation applications. In a study by Chevallier et al. (2004) cloud-affected satellite infrared radiances were successfully assimilated using a variational data assimilation method. They pointed out that for some cloud-affected channels of the METEOSAT and Atmospheric Infrared Sounder (AIRS) instruments, the linearity assumption

might still be valid, thus these channels were easier to assimilate. In Vukicevic et al. (2004, 2006) assimilation of the GOES imager brightness temperatures into a cloud-resolving model was successfully performed, indicating clear benefits in improved cloud analyses and short-term forecasts. It is important to note that the 4-dimensional variational (4D-Var) data assimilation approach used in Vukicevic et al. (2004, 2006) involved an iterative minimization and nonlinear updates of the cloud state variables in fine spatial and temporal resolution, which was helpful to alleviate some of the difficulties due to nonlinearities of the cloud microphysical processes. In Bauer et al. (2006a, b) the approach called 1D-Var+4D-Var was introduced for assimilation of precipitation-affected microwave radiances, which was also adopted for operational application at the European Centre for Medium-Range Weather Forecasts (ECMWF). The two-step approach, where satellite radiances are assimilated by the nonlinear 1D-Var step to produce increments of total column water vapor, and then these increments are assimilated by the linear (so-called incremental) 4D-Var step, has proven better in handling nonlinearities than the incremental 4D-Var approach alone. In Weng et al. (2007) rain-affected satellite microwave radiances from the Advanced Microwave Sounding Unit (AMSU) and the Advanced Microwave Scanning Radiometer (AMSR-E) are assimilated to improve hurricane vortex analysis. They used an approach called hybrid variational (HVAR) scheme, which is similar to the ECMWF 1D-Var+4D-Var approach; however, they employed a different model, the fifth-generation Pennsylvania State University–National Center for Atmospheric Research Mesoscale Model (MM5) and its adjoint (Zou et al. 1998; Zou and Xiao 2000). The data assimilation results indicated improved, more detailed, structures for the hurricane warm core at the upper troposphere and enhanced lower-level wind speed and upper-level divergence, thus highlighting the importance of assimilation of cloudy satellite radiances.

Novel, ensemble-based, data assimilation methods hold a potential to overcome some of the difficulties of cloud and precipitation assimilation, especially because of the use of flow-dependent forecast error covariances and an improved treatment of nonlinearities (due to not using tangent linear and adjoint models). However, applications of the ensemble-based data assimilation methods to remote sensing observations in general are still rare, and the experience with assimilation of cloudy satellite radiances is, to our knowledge, non-existent. Nevertheless, the potential of these methods to further improve the analysis and forecast of clouds and precipitation is evident from the currently available studies (e.g., Liu et al. 2008; Meng and Zhang 2008; Whitaker et al. 2008; Aksoy et al. 2009), which were performed using conventional and/or some remote sensing observations. Therefore, further exploring the ensemble data assimilation methods in cloud and precipitation assimilation should be well worth the effort.

In this study, we report the results of a pilot study, performed to evaluate the potential of the ensemble data assimilation methods to extract maximum information from the future GOES-R radiance observations in cloudy scenes. Through the use of information measures based on the flow-dependent forecast error covariance matrix, we define when and where the observed information is needed the most. This is in the areas where the flow-dependent forecast uncertainty is the largest. We focus on the impact of the observations from the Advanced Baseline Imager (ABI), an instrument that will have significant improvements upon the current GOES imager with more spectral bands, higher spatial and temporal resolution, better navigation, and more accurate calibration (Schmit et al. 2005). It will also have improved temporal and spatial resolution relative to those of the GOES-13/O/P sounders

(Schmit et al. 2008). Before using observed radiances, synthetic ABI radiances at 10.35 μm were assimilated as a first step in this study. The 10.35 μm channel was selected because it is a clean window channel, expected to be sensitive to the hydrometeors at the cloud top, such as cloud ice and snow (Smith et al. 1992; Grasso and Greenwald 2004; Grasso et al. 2008). Therefore, this channel is capable of providing information about cloud microphysical processes at the cloud tops.

This paper is organized as follows. We explain the data assimilation approach employed in this study in Section 2. The synoptic case examined is described in Section 3. Experimental design is given in Section 4, and the results are presented and discussed in Section 5. Finally, the conclusions are drawn and future research directions are outlined in Section 6.

2. Data assimilation approach

a. Basic equations

We employ a variant of the Maximum Likelihood Ensemble Filter (MLEF) data assimilation approach, developed at Colorado State University (Zupanski 2005; Zupanski and Zupanski 2006; Zupanski et al. 2008). This variant includes covariance localization via local domains (e.g., Ott et al. 2004; Yang et al. 2009; Zupanski 2009a, b), thus we call it Local MLEF (LMLEF). The covariance localization is explained in the following subsection while the basic equations of the original MLEF are given in the Appendix.

b. Covariance localization

Covariance localization (e.g., Houtekamer and Mitchell, 2001; Whitaker and Hamill, 2002; Ott et al., 2004) is an effective way to account for the "missing degrees of freedom" in ensemble-based data assimilation systems. By "missing degrees of freedom" we mean that the number of degrees of freedom in the model state variable is much larger than the affordable ensemble size on a given computer. This often happens in applications to complex weather forecast models where the size of the model state variable could easily reach the order of 10^7 – 10^8, while the computationally feasible ensemble size can hardly be increased beyond the order of 10^2. In our experiments the size of the model state vector $\boldsymbol{x}$ is $N_S \approx 3 \times 10^7$, thus it is several orders of magnitude larger than the ensemble sizes employed (16 and 48 members).

We adopted the covariance localization approach based on the so-called "local domains", first proposed by Ott et al. (2004). In this approach, the entire model domain is partitioned into smaller local domains and the analysis solution is defined independently for each local domain. Due to the use of the globally defined forecast error covariance ($\boldsymbol{P}_f$), overlapping local domains, and/or some kind of smoothing, the assumption of "independent local domains" is only partially enforced (e. g., Ott et al. 2004; Yang et al. 2009). The size of the local domains typically reflects the spatial scales of the processes being analyzed (e.g., extratropical or tropical cyclones, ocean currents, carbon transport), thus the assumption that the local domains are, to a degree, independent is considered appropriate. This covariance localization approach was successfully used, in slightly different variants, in many applications (e.g., Hunt et al. 2007; Miyoshi and Yamane 2007; Yang et al. 2009; Zupanski 2009a, b). We use the variant explained in Zupanski (2009a, b). Unlike in the original Ott et

al. (2004) approach, we use non-overlapping local domains, which ensure a well-posed minimization problem in each local domain and provide a straightforward definition of information measures, since each observation belongs to a single local domain and thus contributes to the information measures uniquely (Zupanski 2009a). A disadvantage of using non-overlapping local domains is in possible creations of discontinuities at the boundaries between local domains (which could appear visible in the analysis fields). To eliminate/reduce these discontinuities, smoothing of the analysis weights is applied (e. g., Yang et al. 2009; Zupanski 2009a, b). The use of non-overlapping local domains, in conjunction with the smoothing, provided a satisfactory solution to the two contradictory requirements: to define a well-posed minimization problem over each local domain and to reduce discontinuous transitions from one local domain to another.

3. Model and data

In the data assimilation experiments of this study, we employ, as a forecast model, the non-hydrostatic Weather Research and Forecasting (WRF) model, which uses the Advanced Research WRF (ARW) dynamical core (Skamarock et al. 2005; Wicker and Skamarock 2002). The WRF-ARW model was configured with 15-km grid spacing and 50 vertical levels, covering a domain of approximately 300x300 km centered over Germany. For initial and boundary conditions the National Centers for Environmental Prediction (NCEP) Global Forecasts System (GFS) analyses were used.

In terms of physics, the Betts-Miller-Janjic (BMJ) convective parameterization (Betts 1986, Betts and Miller 1986, Janjic 1994) was utilized, and the Mellor-Yamada-Janjic (Janjic 1994) Planetary Boundary Layer (PBL) scheme was chosen. The effects of radiative transfer for long and short wave radiation were treated by the rapid radiative transfer model (Mlawer et al. 1997) and the Dudhia (1989) scheme, respectively. The Mlawer scheme accounts for multiple bands, trace gasses, and microphysics species, while the Dudhia scheme accounts for simple downward integration and includes an efficient cloudy and clear sky absorption and scattering. For microphysical processes a single-moment, five species, cloud microphysical scheme (Schultz 1995) was used. The scheme of Schultz (1995) has been modified to use the saturation adjustment method of Asai (1965), to slow the melting rate of snow in air slightly warmer than freezing, and to allow for the formation of cloud liquid water in unsaturated grid volumes with lapse rates approaching convective instability.

Regarding the observations, we focus our attention on synthetic radiances from the infrared 10.35 μm channel of the future ABI instrument. We assimilate synthetic observations because the real ABI 10.35 μm radiances are not yet available. The synthetic observations were generated using a different forecast model, the Colorado State University/Regional Atmospheric Modeling System (CSU/RAMS; Cotton et al. 2003). As RAMS includes an advanced two-moment microphysical scheme, it was considered adequate to generate realistic cloud-microphysical variables and, consequently, realistic synthetic 10.35 μm radiances. In Grasso et al. (2008) it was shown that synthetic GOES-R ABI radiances based on the RAMS microphysical variables were quite reasonable. As in Grasso et al. (2008) we create synthetic radiances by applying the satellite observation operator (developed by Greenwald et al. 2002; Grasso and Greenwald 2004) to the RAMS microphysical variables. The observation operator includes a radiative transfer model at infrared wavelengths based on the delta-Eddington 2-stream method (Deeter and Evans 1998) and cloud optical property models at all non-visible

bands, based on modified anomalous diffraction theory (Mitchell 2000; Mitchell 2002; Greenwald et al. 2002), applied to both liquid and ice particles. It also includes a gas extinction model: Optical Path TRANsmittance (OPTRAN; McMillin et al. 1995).

4. Synoptic case

The synoptic case chosen for this study is the extratopical cyclone named Kyrill, which lasted during the period January 15-19, 2007. Due to unusually strong winds, Kyrill caused widespread damage and fatalities in Western Europe, especially in the United Kingdom and in Germany. In figures 1a and 1b we show infrared METEOSAT imagery of Kyrill. The imagery in figure 1a, valid at 1212 UTC 18 January 2007, corresponds to the beginning of the first data assimilation cycle and the imagery in figure 1b, valid at 1912 UTC 18 January 2007, corresponds to the end of the seventh data assimilation cycle of the experiments presented. As the figures indicate, there is a well-developed fast-moving cloud system associated with Kyrill. Note that the METEOSAT data plotted in figures 1a, b is not assimilated in this study. At present, we only use the METEOSAT data to illustrate the location and the extent of the Kyrill cloud system. Assimilation of the infrared METEOSAT radiances will be performed for the same synoptic case in the next stage of this research and reported in a follow up manuscript.

In the experiments of this study, we are focusing on the clouds associated with Kyrill, since our goal is to assimilate cloudy ABI infrared radiance observations. The strong winds of this system make the data assimilation problem more difficult since the clouds are moving quickly and their exact locations are difficult to predict. We anticipate that the use of flow-dependent forecast error covariance would be important for this challenging problem, since it could assign larger uncertainties to the cloud-affected areas.

5. Experimental design

The experimental design corresponds to the so-called “non-identical twins” setup because two different models are used: one (WRF) as a part of data assimilation, and another (RAMS) to create observations. Unlike identical twins, the non-identical twins imply that the forecast models are not perfect, thus achieving experimental conditions resembling assimilation of the real ABI observations.

The WRF model is run over Europe, to capture the extratropical cyclone Kyrill. The horizontal grid spacing of the model is 15 km and there are 50 levels in the vertical. The synthetic 10.35 μm radiances are created with a footprint of 15 km and assimilated into the system every hour (i.e., data assimilation interval was 1 hour). Note that real ABI observations will be available in higher resolution (0.5 to 2 km), thus this experiment simulates the conditions of assimilation of observations that were thinned to approximately match the resolution of the forecast model. Data thinning is often done in routine assimilation of satellite observations at operational meteorological centers to reduce the computational time and storage.

In the experiments presented we used two different ensemble sizes, 16 and 48, and employed two different sets of control variables: with and without cloud ice.

6. Results

a. Selecting control variables

We selected the following model state variables as control variables of data assimilation: potential temperature, specific humidity, and five hydrometeors (cloud water, cloud ice, rain, snow and graupel). We selected these control variables because we expected that they would play significant roles in the cloud-microphysical processes (described by the Schultz microphysical scheme). Then, we performed sensitivity experiments by excluding one control variable at a time and by examining the impact of the absence of this control variable on the data assimilation results. The purpose of these experiments was to evaluate how important is the choice of the control variables for maximizing information from the assimilated observations.

Our sensitivity experiments indicated that cloud ice and snow had more significant impacts, as measured by improvements to both the data assimilation and the first guess forecast, than the remaining three hydrometeors (cloud water, rain and graupel). As an example, in figures 2-4, we summarize the impact of including/excluding cloud ice into the control variable. The impact of snow was similar, but less pronounced. The results shown in figures 2-4 are produced using all other initially selected control variables (potential temperature, specific humidity, cloud water, rain, snow and graupel), with only cloud ice switching on and off. In figure 2 we show the first guess and the analysis of potential temperature at 850 hPa and the corresponding analysis increments (i.e., differences between the analysis and the first guess), obtained in the experiments without and with cloud ice adjustment. In figure 2a the first guess (1-h forecast) is given, in figures 2b and 2c the analyses obtained without and with the cloud ice adjustment are presented, and in figures 2d and 2e the corresponding analysis increments are plotted. By comparing figures 2a and 2b we can see that the potential temperature analysis, obtained in the experiment without cloud ice adjustment, is dramatically different from the background in the area extending from the Alpine region, through northern Mediterranean and southeastern Europe, towards the Scandinavian Peninsula. These differences exceed 25 K in some points, as shown in figure 2d. By examining figures 2a and 2c we can see that the potential temperature analysis, obtained in the experiment with the cloud ice adjustment (figure 2c), is not dramatically different from the background (figure 2a). The analysis increments in figure 2c are much smaller, with a maximum magnitude of 10 K.

The next question we pose is as follows. Are the large potential temperature analysis increments, obtained in the experiment without cloud ice adjustment, effective in making the forecast model closer to the observations? To answer this question, we examine the results shown in figure 3. As seen in figure 3a, the differences between the first guess and the verification ("observed" 10.35 μm radiances) are large, exceeding -0.06 W m^{-2} sr^{-1} cm and +0.05 W m^{-2} sr^{-1} cm in the cloudy areas, which roughly corresponds to the errors between -60 K and +50 K in brightness temperature. The errors of such large magnitudes are due to modeled clouds being shifted with respect to the "observed" clouds. Because the radiative transfer model detects a warm surface instead of a cold cloud top, and vice versa, the brightness temperature differences are large. The first guess and the analysis errors in figure 3 indicate that the WRF-produced clouds are shifted to southeast compared to the RAMS-produced (i.e., "observed") clouds. Also note (figures 1a and 1b), that the real clouds of the

cyclone Kyrill are generally in this area, however, there is a shift with respect to the clouds obtained by any of the two models. The large differences in figure 3 (especially the negative differences) were reduced due to data assimilation; in the experiment with cloud ice adjustment (figure 3c) the model is in better agreement with the "observations" than in the experiment without cloud ice adjustment (figure 3b). These results indicate that the cloud ice adjustment has a more effective impact on improving the analysis than the potential temperature adjustment.

Finally, we show in figure 4a the cloud ice analysis increments at 600 hPa obtained in the experiment with the cloud ice adjustment, and in figures 4b and 4c, a quantitative measure of the amount of information of the assimilated observations, called The Degrees of Freedom for Signal, or DFS (Eq. 6), obtained in the experiments without and with cloud ice adjustment. We present the 600 hPa level as an example of cloud ice increments. Similar increments were obtained at other higher altitude levels, where the amount of cloud ice was non-negligible. We can see, in figure 4a, that the analysis increments, ranging from -0.1 g kg^{-1} to 1.5 g kg^{-1}, are present in central and southeastern Europe, in the area of large disagreement between the model and observations. We do not see analysis increments in the northern Mediterranean region because the 600 hPa temperature is above freezing, preventing cloud ice to form. We can also see, by comparing figures 4b and 4c, that introduction of cloud ice to the control variable results in significantly increased information content of the assimilated observations, even though the same observations were assimilated in both experiments. This is an indication that the appropriate control variable must be chosen in order to extract more information from the same observations.

Note that the DFS, shown in figures 4b and 4c, have blocky structures. The DFS are calculated as total numbers of DFS over each of 25 local domains (blocks), which are the same local domains used for covariance localization (explained in Section 2b). Even though the information measures could be calculated for each model grid point (and the blocky structures would disappear), we calculated them over the local domains, thus to measure the information content contained in each local domain.

In summary, the results presented in figures 2-4 demonstrate that adjusting cloud ice is of substantial importance for assimilation of the 10.35 μm radiances, in cases when cloud ice is present at the cloud tops. These results also indicate that excluding cloud ice from the control variable results in unrealistic changes to the remaining components of the control variable (e.g., potential temperature), since these remaining components could never account, in a physically correct way, for the effect of the cloud ice. This finding confirms indications from earlier studies (e.g., Smith et al. 1992; Grasso and Greenwald 2004; Grasso et al. 2008) that the 10.35 μm channel should be sensitive to cloud ice. For example, in Grasso and Greenwald (2004), it was demonstrated that the 10.35 μm channel should be most sensitive to the hydrometeors at the top of the thunderstorm. Since the top of the thunderstorm mostly contains the cloud ice particles (also called pristine ice), the 10.35 μm channel basically measures the cloud ice in this case. More generally, the results shown in figures 2-4 indicate that it is imperative to include all radiatively active hydrometeors into the control variable for maximizing the benefits of assimilated cloudy radiances and to avoid obtaining degraded data assimilation results due to neglecting some of the important hydrometeors. On the other hand, including microphysical variables to which the radiances have little sensitivity (e.g., rain or graupel) had negligible impact on data assimilation, thus these variables could be either included or excluded from the control variable. In the experiments presented in the remainder

of this paper, we keep all initially selected microphysical variables (potential temperature, specific humidity, cloud water, cloud ice, rain, snow and graupel) as components of the control variable.

b. Data assimilation experiments over multiple data assimilation cycles

In figure 5, we present the Root Mean Square (RMS) errors of the analysis and the first guess, calculated with respect to the RAMS-simulated 10.35 μm radiances, as functions of data assimilation cycles. For reference, the RMS errors of the experiment without data assimilation are also included in figure 5. As seen in figure 5, both the analysis and the first guess are in better agreement with the "truth" than the experiment without data assimilation. Furthermore, the analysis indicates clear improvements with respect to the first guess, and the ensemble size of 48 members has smaller errors than the ensemble size of 16 members. The errors in both data assimilation experiments (with 16 and 48 members) generally decrease with time until around cycle 12, when they saturate at a certain level (with the exceptions of increasing errors from cycle 8 to cycle 12 in some experiments). Note that the errors also decrease, at a slower rate, in the experiment without data assimilation. This is because the influence of the horizontal boundary conditions becomes more dominant with time. Since the same NCEP analyses [from the Gridpoint Statistical Interpolation (GSI) system, Wu et al. 2002] were used to create boundary conditions for both WRF and RAMS, the differences between the two models decrease with time, and consequently the differences between the WRF-simulated and the RAMS-simulated (i.e., "observed") radiances decrease too. In summary, figure 5 indicates a positive impact of data assimilation of the 10.35 μm synthetic radiances on the analysis and short term forecast and a positive impact of the increased ensemble size, over 17 data assimilation cycles. We have not run data assimilation experiments beyond 17 data assimilation cycles since the analysis and forecast errors saturated around cycle 12 in all experiments.

We also show, in figure 6, the histogram of error distributions for the data assimilation experiment with 48 ensemble members and the experiment without data assimilation. By comparing the results from cycles 1 and 7, shown in panels (a) and (b), respectively, we can see that the errors are clustering around zero in the later cycle (i.e., cycle 7), indicating improvements in the first guess, the analysis and the no assimilation experiment. The errors from the analysis and the first guess cluster more around zero than the errors of the experiment without assimilation (note outliers in the positive errors for the no assimilation case). These results confirm a positive impact of data assimilation on the analysis and short-term forecast improvements.

One can also see in figures 6a, b that the errors follow a Gaussian distribution reasonably well. This is an indication that the commonly used assumption about Gaussian errors (and also used in this study) is reasonable in this case. Note, however, that cloudy satellite radiances could often depart from Gaussian distribution (e.g., could follow log-normal distribution: cf. Grasso et al. 2009). In such cases a different cost function needs to be minimized as proposed in Fletcher and Zupanski (2006a, b).

We now examine whether the actual analysis errors are in agreement with the estimated analysis uncertainty. Examples of difference fields, calculated between the model-simulated radiances and the "observed" radiances at 10.35 μm and the corresponding analysis

uncertainty σ_{obs}^{a} (Eq. 7) are shown in figures 7 and 8. The differences are plotted for data assimilation cycle 7, valid at 1900 UTC 18 Jan 2007, and they correspond to the experiment without assimilation (i.e., old forecast, figure 7a), the first guess (1-h forecast after data assimilation, figure 7b) and the analysis (figure 7c). As indicated before, there are large discrepancies between the model and the "observations" in areas over the Alps, the northern Mediterranean and southeastern Europe. These discrepancies remain relatively large throughout the entire period (17 data assimilation cycles); however, they are decreasing with time in both experiments (with and without data assimilation), as the RMS errors in figure 5 indicate. Nevertheless, we can still see a pronounced dipole of positive-negative differences [with maxima exceeding -0.06 or +0.05 W m^{-2} sr^{-1} cm] extending over the Alps, the northern Mediterranean and southeastern Europe in figure 7a (experiment without data assimilation). The impact of data assimilation is to significantly reduce the magnitudes of the large differences for the first guess (figure 7b) and to a lesser extent the analysis (figure 7c). Note, however, that the large differences still remain in this area and they appear in some additional areas (e.g., over the northern part of the Pyrenean peninsula). Due to the non-identical twins setup we do not expect that the differences should eventually become negligible throughout the entire model domain, as they would in the identical twins setup. We do expect, however, that the method should be able to assign realistic (i.e., large) uncertainties to the points where these differences are large.

As we can see in figure 8a, the analysis uncertainty is generally larger in the areas where the analysis-minus-observations differences are larger (in figure 7c). We can also see that the magnitudes of the analysis errors are in good agreement: for example, there are areas of large analysis errors, exceeding ±0.04 W m^{-2} sr^{-1} cm, in figure 7c (e.g., Alpine region, northern Mediterranean, southeastern and northeastern Europe), and the estimated analysis uncertainty is generally in the range 3.5-5 W m^{-2} sr^{-1} cm in these areas. These results confirm that the LMLEF calculated analysis uncertainty is a good estimate of the actual analysis errors in terms of both the magnitude and structure of the errors. In figure 8b we show an information measure, DFS (Eq. 6), calculated in data assimilation cycle 7. As the figure indicates, areas (i.e., blocks) with large values of DFS generally coincide with the large analysis uncertainty in figures 7c and 8a. The results shown in figures 8a and 8b confirm the flow-dependent character of the analysis error covariance and the information measures, because the analysis errors and the information measures follow flow characteristics of the Kyrill cloud system. Flow-dependent analysis and forecast error covariance matrices are considered important ingredients of advanced data assimilation systems.

Let us now examine the vertical cross section taken along the line AB (the location of the cross section is shown in figures 7 and 8). As seen in figure 7, the cross section is taken in the area where the differences between the model and the "observations" are large and they also change sign within the cross section. The analysis uncertainty and the information measure (DFS) are also large in this area (see figure 8). We present the vertical cross section of potential temperature and cloud ice in figure 9, including "observations" and model results. We can see that the model-produced potential temperature is generally colder in the lower levels compared to the "observations", and the opposite is true for the upper levels. We also see large differences between the modeled and the "observed" cloud ice in both the magnitudes and the locations of the maximum values. These differences, even though large, are reasonable: we are comparing two different forecast models, which have different dynamical cores and microphysical schemes. Nevertheless, the impact of data assimilation

should be in reducing, to some extent, these large differences. By comparing the experiment without data assimilation (figure 9b) with the 1-h first guess forecast initialized by data assimilation (figure 9c) and the analysis (figure 9d) we can see that the impact of data assimilation is relatively small on the potential temperature, but quite pronounced on the cloud ice. For example, the maximum of the cloud ice has moved westward in the first guess forecast (figure 9c) and the analysis (figure 9d), which is in better agreement with the "observations" (figure 9a) than the maximum obtained in the experiment without data assimilation (figure 9b). Additionally, the vertical structure of the cloud ice is in generally better agreement with the "observations" for the analysis as compared to the first guess, which is evidence of the analysis improvement with respect to the first guess. In conclusion, the impact of data assimilation is seen in more significant changes (which were also in the right direction) in the cloud ice than in the potential temperature. These results are reasonable, since the 10.35 μm radiance is expected to be more sensitive to the cloud ice than to any other microphysical variable under the conditions of this experiment (also confirmed in Grasso and Greenwald 2004 for a similar window channel of 10.7 μm).

7. Conclusions

In this study we assimilated synthetic GOES-R ABI radiances at 10.35 μm in cloudy conditions to evaluate the potential impact of these observations on improving model-simulated clouds. In particular, we were interested in extracting maximum information from such observations by taking into account when and where this information is needed the most. Our criteria for defining when and where the information is needed the most were based on information theory and the use of information measures (such as DFS). We have performed cycled data assimilation experiments for the case of the extratropical cyclone Kyrill. This case was especially challenging because of the large errors in model-simulated radiances due to spatially shifted clouds.

The experimental results indicated that the same GOES-R observations could bring varying amounts of information, depending on the choice for the control variable in data assimilation. When cloud ice was included into the control variable, the information content of data, as measured by DFS, was significantly increased and the data assimilation results were much improved compared to the case without including cloud ice into the control variable. The impact of data assimilation was also seen in much more significant changes to the cloud ice than to other model state variables, such as potential temperature. This is not surprising, since the 10.35 μm channel is expected to be sensitive to the hydrometeors at the cloud top, but not sensitive to the air temperature or potential temperature (e.g., Smith et al. 1992; Grasso and Greenwald 2004). Therefore, our results indicated that it is imperative to include all radiatively active hydrometeors into the control variable for maximizing the benefits of assimilated cloudy radiances and to avoid obtaining degraded data assimilation results due to neglecting some of the important hydrometeors. On the other hand, microphysical variables to which the radiances have little sensitivity (e.g., rain or graupel) could be either included or excluded from the control variable.

The data assimilation and short term forecast results over multiple data assimilation cycles have clearly indicated improvements due to assimilation of the GOES-R ABI radiance "observations", compared to the experiment without data assimilation. The experimental results also indicated that the flow-dependent DFS used in this study realistically reflect the

actual forecast uncertainty: the values of DFS were the largest in the areas of largest forecast errors. This is a confirmation that the data assimilation method used in this study has the capability to maximize information content of the assimilated observations.

In future work, we plan to further evaluate the capability of the LMLEF approach, and the ensemble-based data assimilation methods in general, to extract maximum information from real satellite observations. For this purpose we plan to assimilate cloudy radiances similar to the future ABI radiances (e. g., from the METEOSAT Second Generation – MSG and/or the Atmospheric Infrared Sounder – AIRS instruments).

Appendix: Basic equations of the MLEF

The MLEF seeks a maximum likelihood solution of the posterior Probability Density Function (PDF), which is equivalent to seeking a minimum of the following cost function (under the standard assumption of Gaussian PDFs for the observation and forecast errors)

$$J(\boldsymbol{x}) = \frac{1}{2}\left(\boldsymbol{x}-\boldsymbol{x}^f\right)^T \boldsymbol{P}_f^{-1}\left(\boldsymbol{x}-\boldsymbol{x}^f\right) + \frac{1}{2}\left[\boldsymbol{y}-H(\boldsymbol{x})\right]^T \boldsymbol{R}^{-1}\left[\boldsymbol{y}-H(\boldsymbol{x})\right]. \quad (1)$$

The cost function (1) measures the differences between the model and the observations, where vector $\boldsymbol{y}$ of dimension N_{obs} (number of observations) is the observation vector, vector $\boldsymbol{x}$ of dimension N_S (model state dimension) is the model state vector, non-linear operator H is an observation operator, matrix $\boldsymbol{R}$ is the observation error covariance and matrix $\boldsymbol{P}_f$ is the forecast error covariance. The index f refers to the forecast (used as a first guess). The matrix $\boldsymbol{P}_f$ is defined in a subspace spanned by ensemble forecast perturbations as

$$\boldsymbol{P}_f^{1/2} = \left[\boldsymbol{p}_1^f \quad \boldsymbol{p}_2^f \quad \cdot \quad \cdot \quad \boldsymbol{p}_{N_E}^f\right] \qquad \boldsymbol{p}_i^f = M(\boldsymbol{x}^a + \boldsymbol{p}_i^a) - M(\boldsymbol{x}^a), \quad (2)$$

where M denotes the nonlinear forecast model, the superscript a refers to the analysis, and N_E is the number of ensembles. The vectors $\boldsymbol{p}_i^a$ and $\boldsymbol{p}_i^f$ represent columns of the square roots of the analysis and forecast error covariances, respectively. The square root of the analysis error covariance is defined at the analysis solution $\boldsymbol{x}^a$ as

$$\boldsymbol{P}_a^{1/2} = \boldsymbol{P}_f^{1/2}\left[\boldsymbol{I}_{N_E} + \left(\boldsymbol{Z}(\boldsymbol{x}^a)\right)^T \boldsymbol{Z}(\boldsymbol{x}^a)\right]^{-1/2}, \quad (3)$$

where $\boldsymbol{I}_{N_E}$ is an $N_E \times N_E$ identity matrix and the matrix $\boldsymbol{Z}(\boldsymbol{x}^a)$ is the observation perturbation matrix at the analysis solution, defined by the following equation

$$\boldsymbol{Z}(\boldsymbol{x}^a) = \left[z_1(\boldsymbol{x}^a) \quad z_2(\boldsymbol{x}^a) \quad \cdot \quad \cdot \quad z_{N_E}(\boldsymbol{x}^a)\right] \qquad z_i(\boldsymbol{x}^a) = \boldsymbol{R}^{-1/2}\left[H(\boldsymbol{x}^a + \boldsymbol{p}_i^f) - H(\boldsymbol{x}^a)\right]. \quad (4)$$

The inverse square root calculation in (3) is obtained via eigenvalue decomposition of the matrix $\boldsymbol{I}_{N_E} + \boldsymbol{Z}(\boldsymbol{x}^a)^T \boldsymbol{Z}(\boldsymbol{x}^a)$. It is calculated as a symmetric square root, which is unique (e.g., Wang et al. 2004; Zupanski 2005; Wei et al. 2006).

We also calculate, as a diagnostic, the so-called information matrix $\boldsymbol{C}$, of dimensions $N_E \times N_E$, defined in ensemble subspace as

$$\boldsymbol{C} = \boldsymbol{Z}(\boldsymbol{x}^a)^T \boldsymbol{Z}(\boldsymbol{x}^a) \ , \tag{5}$$

which we use to calculate information measures, such as Degrees of Freedom for Signal (DFS) defined as (e.g., Shannon and Weaver 1949; Rodgers, 2000; Zupanski et al., 2007)

$$DFS = \sum_{i=1}^{N_E} \frac{\lambda_i^2}{(1+\lambda_i^2)} \ , \tag{6}$$

where index *i* denotes an ensemble member and λ_i^2 are eigenvalues of the information matrix $\boldsymbol{C}$.

As an additional diagnostic, we also calculate analysis uncertainty in observation locations and in terms of the observed variable (10.35 μm radiance in the experiments presented) to be able to compare it with the actual analysis uncertainty, defined by the differences between the analysis and the "truth" (the "truth" being defined by a different forecast model in our "non-identical twins" experimental setup). The analysis uncertainty, defined as the standard deviation of the analysis errors (σ_{obs}^a), is calculated using the following formula

$$\sigma_{obs}^a = \left\{ diag\left[\boldsymbol{R}^{1/2} \boldsymbol{G}\left(\boldsymbol{x}^a\right) \boldsymbol{G}\left(\boldsymbol{x}^a\right)^T \boldsymbol{R}^{T/2} \right] \right\}^{1/2} , \tag{7}$$

where the $N_{obs} \times N_E$ matrix $\boldsymbol{G}$ consists of column perturbation vectors $\boldsymbol{g}_i(\boldsymbol{x}^a)$ defined by:

$$\boldsymbol{G}(\boldsymbol{x}^a) = \left[\boldsymbol{g_1}(\boldsymbol{x}^a) \quad \boldsymbol{g_2}(\boldsymbol{x}^a) \quad \cdot \quad \cdot \quad \boldsymbol{g}_{N_E}(\boldsymbol{x}^a) \right] \qquad \boldsymbol{g}_i(\boldsymbol{x}^a) = \boldsymbol{R}^{-1/2} \left[H(\boldsymbol{x}^a + \boldsymbol{p}_i^a) - H(\boldsymbol{x}^a) \right]. \tag{8}$$

Note similarity between equations (8) and (4): the only difference is that for calculating matrix $\boldsymbol{G}$ the analysis perturbations $\boldsymbol{p}_i^a$ are used, while for matrix $\boldsymbol{Z}$ the forecast perturbations $\boldsymbol{p}_i^f$ are employed. Note also that both the forecast perturbation vectors $\left[\boldsymbol{z}_i(\boldsymbol{x}^a) \right]$ and the analysis perturbation vectors $\left[\boldsymbol{g}_i(\boldsymbol{x}^a) \right]$ are calculated using non-linear observation operators *H*, in accordance with the non-linear character of the MLEF algorithm.

The equations (1) – (6) are solved employing an iterative minimization (Zupanski 2005). In addition, as demonstrated in Zupanski et al. (2008), assumptions of differentiability, used in the standard gradient-based minimization methods, were not necessary, thus this approach is considered adequate for non-linear and discontinuous cloud microphysical processes, which play an important role in the experiments of this study.

Acknowledgements

This work was supported by the NOAA/NESDIS GOES-R Risk Reduction Program, Grant No. NA17RJ1228 and the National Science Foundation Collaboration in Mathematical Geosciences Program, Grant No. ATM-0327651. Our gratitude is also extended to National Center for Atmospheric Research (NCAR) for the computational time on the IBM Bluefire supercomputer. The views, opinions, and findings in this report are those of the authors and should not be construed as an official NOAA and or U. S. Government position, policy, or decision.

Figure captions

Figure 1. METEOSAT infrared satellite imagery of Kyrill, from 18 January 2007 at (a) 1212 UTC, and (b) 1912 UTC.

Figure 2. Potential temperature at 850 hPa and the corresponding analysis increments (i.e., differences between the analysis and the first guess), obtained in the experiments without and with cloud ice adjustment. The first guess (1-h forecast) is shown in (a), the analysis without cloud ice adjustment is plotted in (b) and the analysis with cloud ice adjustment is given in (c). The corresponding analysis increments are shown in (d) and (e) for the experiments without and with cloud ice adjustment, respectively.

Figure 3. Differences calculated between the model-simulated and the "observed" 10.35 μm radiances for (a) the first guess forecast, (b) the analysis without cloud ice adjustment and (c) the analysis with cloud ice adjustment. The differences correspond to the end of the first data assimilation cycle (1300 UTC 18 Jan 2007). Units for radiances are W m^{-2} sr^{-1} cm.

Figure 4. (a) Cloud ice analysis increments (in units of g kg^{-1}) at 600 hPa level obtained in the experiment with the cloud ice adjustment in the first data assimilation cycle (1300 UTC 18 Jan 2007). Information content of the assimilated observations (DFS, Eq. 6) calculated in the same data assimilation cycle is shown for the experiment without cloud ice adjustment in (b) and for the experiment with cloud ice adjustment in (c). The DFS in (b) and (c) are non-dimensional quantities, which count the total number of independent pieces of information per local domain (block).

Figure 5. RMS errors of the analysis (ANL, dashed lines) and the first guess (FG, solid lines) calculated with respect to the RAMS-simulated 10.35 μm radiances and plotted as functions of data assimilation cycles. Results from the experiments with 16 and 48 ensemble members are shown. For reference, the RMS errors of the experiment without data assimilation (NO_OBS, solid line) are also included. Units for radiances are W m^{-2} sr^{-1} cm.

Figure 6. Probability histogram of the errors of the 10.35 μm radiances, calculated with respect to RAMS-simulated radiances, for the first guess (FG), the analysis (ANL) and the experiment without assimilation (NO_OBS). Data assimilation experiments using ensemble

size of 48 members are shown. Results from first (a) and seventh (b) data assimilation cycle are presented. Units for radiances are W m^{-2} sr^{-1} cm.

Figure 7. Differences, corresponding to the end of the seventh data assimilation cycle (1900 UTC 18 Jan 2007), calculated between the model-simulated the "observed" 10.35 μm radiances are plotted for (a) the experiment without data assimilation (i.e., old forecast), (b) 1-h forecast used as a first guess in data assimilation, and (c) the analysis. The units for radiances are W m^{-2} sr^{-1} cm. Line AB indicates location of the vertical cross section shown in figure 9.

Figure 8. Analysis uncertainty for the 10.35 μm radiances (σ^{a}_{obs} , Eq. 7) is plotted in (a) and the corresponding DFS (Eq. 6) is shown in (b). The results are given for the seventh data assimilation cycle, thus are comparable to the results in figure 7. The units for radiances are W m^{-2} sr^{-1} cm, however the values are scaled by 100.

Figure 9. Vertical cross section taken along the line AB shown in figures 7 and 8. Potential temperature (shading) and cloud ice (contours) are shown in the figure. The results are valid at the end of seventh data assimilation cycle (1900 UTC 18 January 2007). The "observations" (RAMS forecasts) are given in panel (a), the forecast results from the experiment without assimilation are shown in (b), the 3-h background in (c) and the analysis in (d). Units for potential temperature are K and for cloud ice g kg^{-1}.

References

Aksoy, A., Dowell, D.C. and Snyder C., 2009, A multi-scale comparative assessment of the ensemble Kalman filter for assimilation of radar observations. Part I: Storm-scale analysis. *Mon. Wea. Rev.*, (*In Press*).

Andersson E., Bauer P., Beljaars A., Chevallier F., Holm E., Janiskova M., Kallberg P., Kelly G.A., Lopez P., McNally A.P., Moreau E., Simmons A.J., Thepaut J.-N. and Tompkins A.M., 2005, Assimilation and modeling of the atmospheric hydrological cycle in the ECMWF forecasting system. *Bull. Am. Meteorol. Soc.* **86**: 387–402.

Asai, T., 1965, A numerical study of the air-mass transformation over the Japan Sea in winter. *J. Meteorol. Soc. Jpn.,* **43,** 1-15.

Betts, A.K., 1986, A new convective adjustment scheme. Part I: Observational and theoretical basis. *Quart. J.Roy. Meteor.* Soc., **112**, 677-692.

Betts, A.K. and Miller, M.J., 1986, A new convective adjustment scheme Part II: Single column tests using GATE wave, BOMEX, and arctic air-mass data sets. *Quart J. Roy. Meteor. Soc*., **112**, 693-709.

Bauer P., Lopez, P., Benedetti, A., Salmond, D., and Moreau, E., 2006a, Implementation of 1D+4D-Var assimilation of precipitation-affected microwave radiances in precipitation at ECMWF. I: 1D-Var. *Quart. J. Roy. Meteor. Soc.*, **132**, 2227–2306.

Bauer P., Lopez, P., Benedetti, A., Salmond, D., Saarinen, S. and Bonazzola, M., 2006b, Implementation of 1D+4D-Var assimilation of precipitation-affected microwave radiances in precipitation at ECMWF. II: 4D-Var. *Quart. J. Roy. Meteor. Soc.*, **132**, 2307–2332.

Carton, J.A. and Giese, B.S., 2008, A reanalysis of ocean climate using Simple Ocean Data Assimilation (SODA). *Mon. Wea. Rev.*, **136**, 2999–3017.

Chevallier, F., Lopez, P., Tompkins, A., Janisková, M. and Moreau, E., 2004, The capability of 4D-Var systems to assimilate cloud-affected satellite infrared radiances. *Quart. J. Roy. Meteor. Soc.,* **130,** 917–932.

Cotton, W.R., Pielke, R.A.Sr., Walko, R.L., Liston, G.E., Tremback, C.J., Jiang, H., Mcanelly, R.L., Harrington, J.Y., Nicholls, M.E., Carrio, G.G. and Mcfadden, J.P., 2003, RAMS 2001: Current status and future direction. *Meteorology and Atmospheric Physics*, **82**, 5–29.

Deeter, M. and Evans, K.F., 1998, A hybrid Eddington-single scatter radiative transfer model for computing radiances from thermally emitting atmospheres. *J. Quant. Spect. Rad. Transfer*, **60**, 635-648.

Dudhia, J., 1989, Numerical study of convection observed during the winter monsoon experiment using a mesoscale two-dimensional model, *J. Atmos. Sci*., **46**, 3077–3107.

Errico, R., Mahfouf, J.-F. and Bauer, P., 2007: Issues regarding the assimilation of cloud and precipitation data. *J. Atmos. Sci.,* **64,** 3785–3798.

Fletcher, S.J. and Zupanski, M. 2006a: A hybrid multivariate normal and lognormal distribution for data assimilation. *Atmos. Sci. Lett.,* **7,** 43-46.

Fletcher, S.J. and Zupanski, M. 2006b: A data assimilation method for lognormally distributed observational errors. *Quart. J. Roy. Meteor. Soc.,* **132,** 2505-2519.

Grasso, L.D. and Greenwald, T., 2004, Analysis of 10.7 µm brightness temperatures of a simulated thunderstorm with two-moment microphysics. *Mon. Wea. Rev*., **132**, 815-825.

Grasso, L.D., Sengupta and DeMaria, M., 2009, Comparison between Observed and Synthetic 6.5 and 10.7 µm GOES-12 Imagery of Thunderstorms. *International Journal of Remote Sensing*, (*In Press*).

Grasso, L.D., Sengupta, M., Dostalek, J.F., Brummer, R. and DeMaria, M., 2008, Synthetic satellite imagery for current and future environmental satellites. *International Journal of Remote Sensing*, **29**, 4373-4384.

Greenwald, T.J., Hertenstein, R. and Vukicevic, T., 2002, An all-weather observational operator for radiance data assimilation with mesoscale forecast models. *Mon. Wea. Rev.*, **130**, 1882-1897.

Hollingsworth, A., Engelen, R.J., Textor, C., Benedetti, A., Boucher, O., Chevallier, F., Dethof, A., Elbern, H., Eskes, H., Flemming, J., Granier, C., Kaiser, J.W., Morcrette, J.J., Rayner, P., Peuch, V.H., Rouil, L., Schultz, M.G., Simmons, A.J. and The GEMS Consortium, 2008, Toward a monitoring and forecasting system for atmospheric composition: The GEMS project. *Bull. Amer. Meteor. Soc.*, **89**, 1147–1164.

Hou, A.Y. and Zhang, S.Q., 2007, Assimilation of precipitation information using column model physics as a weak constraint. *J. Atmos. Sci.*, **64**, 3865–3878.

Houtekamer, P.L. and Mitchell, H.L., 2001, A sequential ensemble Kalman filter for atmospheric data assimilation. *Mon. Wea. Rev.,* **129**, 123–137.

Houtekamer P.L., Mitchell, H.L., Pellerin, G., Buehner, M., Charron, M., Spacek, L. and Hansen, B., 2005, Atmospheric data assimilation with an ensemble Kalman filter: Results with real observations. *Mon. Wea. Rev.*, **133**, 604–620.

Hunt, B.R., Kostelich, E.J. and Szunyogh, I., 2007, Efficient datra assimilation for

spatiotemporal chaos: A local ensemble transform Kalman filter. *Physica D*, **230**, 112-126.

Janjic, Z.I., 1994, The step-mountain Eta coordinate model: Further developments of the convection closure schemes. *Mon. Wea. Rev.*, **122**, 927-945.

Jung, J.A., Zapotocny, T.H., Le Marshall, J.F. and Treadon, R.E., 2008: A Two-Season Impact Study of NOAA Polar-Orbiting Satellites in the NCEP Global Data Assimilation System. *Wea. Forecasting*, **23**, 854–877.

Keppenne, C.L., Rienecker, M.M., Jacob, J.P. and Kovach, R., 2008, error covariance modeling in the GMAO ocean ensemble Kalman filter. *Mon. Wea. Rev.*, **136**, 2964–2982.

L'Ecuyer T., Gabriel, P., Leesman, K., Cooper, S. and Stephens, G., 2006, Objective assessment of the information content of visible and infrared radiance measurements for cloud microphysical property retrievals over the global oceans. Part 1: Liquid clouds. *J. Appl. Meteor. Climatol.*, **45**, 20–41.

Lin, X., Zhang, S.Q. and Hou, A.Y., 2007, Variational assimilation of global microwave rainfall retrievals: Physical and dynamical impact on GEOS analyses. *Mon. Wea. Rev.*, **135**, 2931–2957.

Liu, H., Anderson, J., Kuo, Y.H., Snyder, C. and Caya, A., 2008, Evaluation of a nonlocal quasi-phase observation operator in assimilation of CHAMP radio occultation refractivity with WRF. *Mon. Wea. Rev.*, **136**, 242–256.

McMillin, L.M., Crone, L.J., Goldberg, M.D. and Kleespies, T.J., 1995, Atmospheric transmittance of an absorbing gas, 4. OPTRAN: A computationally fast and accurate transmittance model for absorbing gases with fixed and variable mixing ratios at variable viewing angles. *Appl. Opt.*, **34**, 6269-6274.

Meng Z. and Zhang F., 2008, Tests of an ensemble Kalman filter for mesoscale and regional-scale data assimilation. Part IV: Comparison with 3DVAR in a month-long experiment. *Mon. Wea. Rev.*, **136**, 3672-3682.

Migliorini, S., Piccolo, C. and Rodgers, C.D., 2008, Use of the information content in satellite measurements for an efficient interface to data assimilation. *Mon. Wea. Rev.*, **136**, 2633–2650.

Mitchell, D.L., 2000, Parameterization of the Mie extinction and absorption coefficients for water clouds. *J. Atmos. Sci.*, **57**, 1311-1326

Mitchell, D.L., 2002, Effective diameter in radiation transfer: General definitions, applications, and limitations. *J. Atmos. Sci.*, **59**, 2330-2346.

Miyoshi T. and Yamane, S., 2007, Local ensemble transform Kalman filtering with an AGCM at T159/L60 resolution. *Mon. Wea. Rev.*, **135**, 3841–3861.

Mlawer, E.J., Taubman, S.J., Brown, P.D., Iacono, M.J. and Clough, S.A., 1997, Radiative transfer for inhomogeneous atmosphere: RRTM, a validated correlated-k model for the longwave. J. Geophys. Res., 102 (D14), 16663–16682.

Ott, E., Hunt, B.R., Szunyogh, I., Zimin, A.V., Kostelich, E.J., Corazza, M., Kalnay, E., Patil, D.J. and Yorke, J.A., 2004, A local ensemble Kalman filter for atmospheric data assimilation. *Tellus*, **56A**, 273-277.

Reichle R.H., 2007, Comparison and assimilation of global soil moisture retrievals from the Advanced Microwave Scanning Radiometer for the Earth Observing System (AMSR-E) and the Scanning Multichannel Microwave Radiometer (SMMR). *J. Geophys. Res.*, **112**, D09108, doi:10.1029/2006JD008033.

Rodgers, C.D., 2000: *Inverse Methods for Atmospheric Sounding: Theory and Practice*. World Scientific, 238 pp.

Shannon, C.E. and Weaver, W., 1949, *The Mathematical Theory of Communication*. University of Illinois Press, 144 pp.

Schmit, T.J., Gunshor, M.M., Menzel, W.P., Gurka, J.J., Li, J. and Bachmeier, S., 2005, Introducing the next-generation Advanced Baseline Imager on GOES-R. *Bull. Amer. Meteorol. Soc.*, **86**, 1079-1096.

Schmit, T.J., Li, J., Gurka, J.J., Goldberg, M.D., Schrab, K.J., Li, J. and Feltz, W.F., 2008, The GOES-R advanced baseline imager and the continuation of current sounder products. *J. Appl. Meteor. and Climat.*, **47**, 2696-2711.

Schultz, 1995, An explicit cloud physics parameterization for operational numerical weather prediction. *Mon. Wea. Rev*., **123**, 3331-3343.

Skamarock W.C., Klemp, J.B., Dudhia, J., Gill, D.O., Barker, D.M., Wang, W. and Powers, J.G., 2005, A description of the advanced research WRF Version 2. NCAR Tech. Note 5, 22 pp.

Smith, W. L., X. L. Ma, S. A. Ackerman, H. E. Revercomb, and R. O. Knuteson, 1992: Remote sensing cloud properties from high-spectral resolution infrared observations. *J. Atmos. Sci.,* **50**, 1708-1720.

Vukicevic, T., Greenwald, T., Zupanski, M., Zupanski, D., Vonder Haar, T. and A.S. Jones, 2004, Mesoscale Cloud State Estimation from Visible and Infrared Satellite Radiances. *Mon. Wea. Rev.*, **132**, 3066–3077.

Vukicevic, T., Sengupta, M., Jones, A. and Vonder Haar, T., 2006, Cloud resolving data assimilation: Information content of IR window observations and uncertainties in estimation. *J. Atmos. Sci.,* **63,** 901–919.

Wang X., C. H. Bishop, and S.J. Julier, 2004: Which is better, an ensemble of positive/negative pairs or a centered spherical simplex ensemble? *Mon. Wea. Rev.* **132**, 1590–1605.

Wei M., Z. Toth R. Wobus, Y. Zhu, C. H. Bishop, and X. Wang, 2006: Ensemble Transform Kalman Filter-based ensemble perturbations in an operational global prediction system at NCEP. *Tellus* **58A**: 28 – 44.

Weng F., T. Zhu, and B. Yan, 2007: Satellite data assimilation in numerical weather prediction models. Part II: Uses of rain-affected radiances from microwave observations for hurricane vortex analysis. *J. Atmos. Sci.*, **64**, 3910–3925.

Wicker L.J. and Skamarock, W.C., 2002, Time-splitting methods for elastic models using forward time schemes. *Mon. Wea. Rev.*, **130**, 2088–2097.

Whitaker, J.S. and Hamill, T.M., 2002, Ensemble data assimilation without perturbed observations. *Mon. Wea. Rev*., **130**, 1913-1924.

Whitaker, J.S., Hamill, T.M., Wei, X., Song, Y. and Toth, Z., 2008, Ensemble data assimilation with the NCEP global forecast system. *Mon. Wea. Rev.*, **136**, 463-482.

Wu W.-S., R. J. Purser, and D. F. Parrish, 2002: Three-dimensional variational analysis with spatially inhomogeneous covariances. *Mon. Wea. Rev.*, **130**, 2905–2916.

Yang, S.-C., E. Kalnay, B. Hunt, and N. E. Bowler, 2009: Weight interpolation for efficient data assimilation with the Local Ensemble Transform Kalman Filter, *Q. J. R. Meteorol. Soc*., (*In Press*).

Zou, X., Huang, W. and Xiao, Q., 1998, A user's guide to the MM5 adjoint modeling system. NCAR Tech. Note TN-437_IA, 94 pp. [Available from NCAR Publications Office,

P.O. Box 3000, Boulder, CO 80307-3000.]

Zou, X., Vandenberghe, P., Wang, B., Gorbunov, M.E., Kuo, Y.-H., Sokolovskiy, S., Chang, J.C., Sela, J.G. and Anthes, R.A., 1999, A raytracing operator and its adjoint for the use of GPS/MET refraction angle measurements. *J. Geophys. Res.*, **104**, 22301-22318.

Zou, X. and Xiao, Q., 2000, Studies on the initialization and simulation of a mature hurricane using a variational bogus data assimilation scheme. *J. Atmos. Sci.,* **57,** 836–860.

Zupanski, D., Hou, A.Y., Zhang, S.Q., Zupanski, M., Kummerow, C.D. and Cheung, S.H., 2007, Application of information theory in ensemble data assimilation. *Q. J. R. Meteorol. Soc*., **133**, 1533-1545.

Zupanski D., 2009a, Information Measures in Ensemble Data Assimilation. In *Data Assimilation for Atmospheric, Oceanic, and Hydrologic Applications*, S.-K. Park, and L. Xu, Eds., Springer (*In Press*).

Zupanski, D. and Zupanski, M., 2006, Model Error Estimation Employing Ensemble Data Assimilation Approach. *Mon. Wea. Rev*., **134**, 1337-1354.

Zupanski, M., 2005, Maximum Likelihood Ensemble Filter: Theoretical Aspects. *Mon. Wea. Rev*., **133**, 1710–1726.

Zupanski, M., Navon, I.M. and Zupanski, D., 2008, The Maximum Likelihood Ensemble Filter as a non-differentiable minimization algorithm. *Q. J. R. Meteorol. Soc*., **134**, 1039-1050.

Zupanski, M., 2009b, Theoretical and Practical Issues of Ensemble Data Assimilation in Weather and Climate. In *Data Assimilation for Atmospheric, Oceanic, and Hydrologic Applications*, S.-K. Park, and L. Xu, Eds., Springer (*In Press*).

(a)

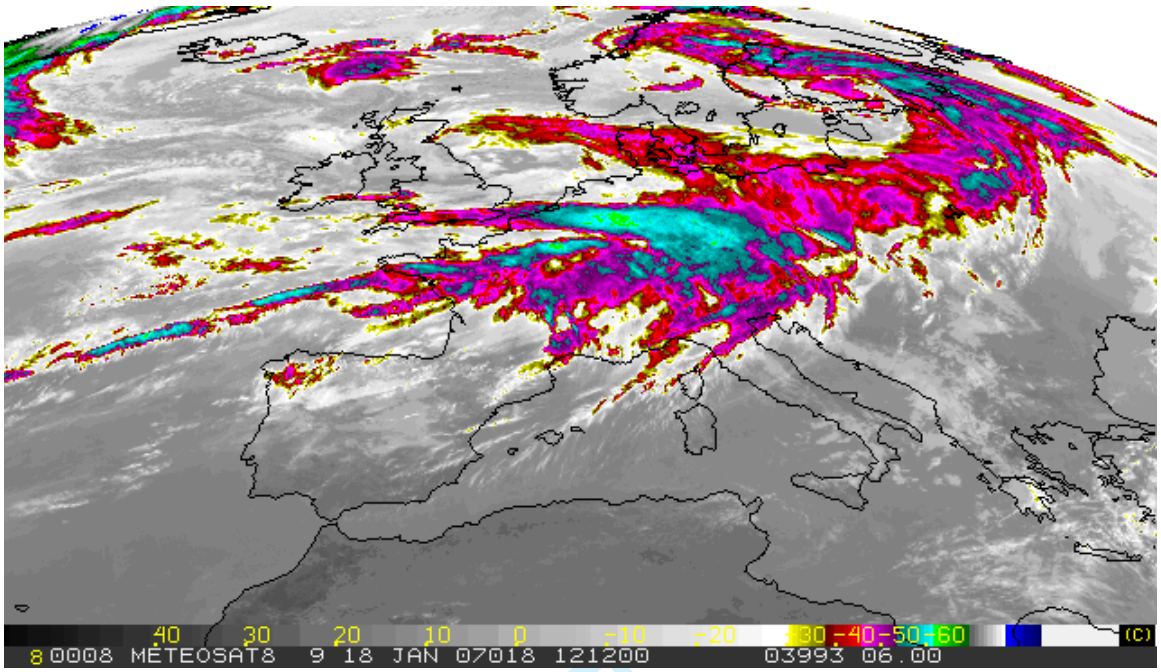

(b)

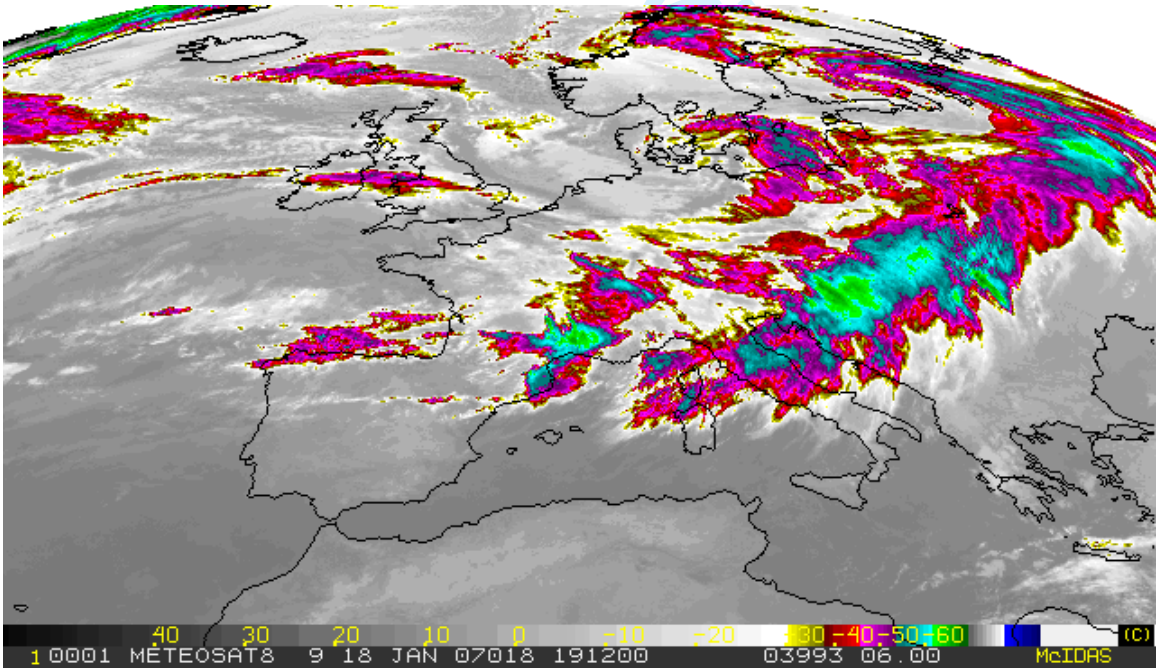

Figure 1. Meteosat infrared satellite imagery of Kyrill, from 18 January 2007 at (a) 1212 UTC, and (b) 1912 UTC

(a)

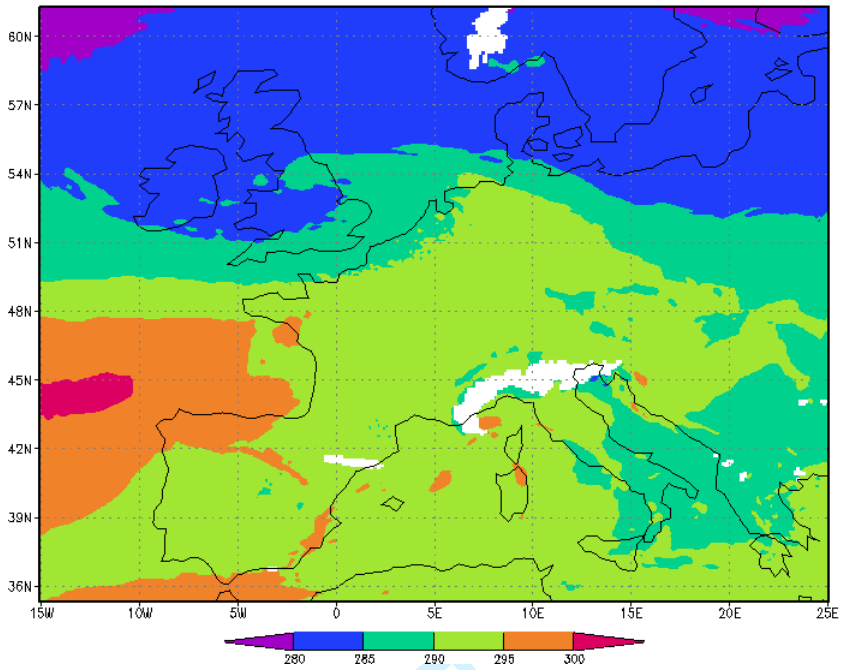
60N
57N
54N
51N
48N
45N
42N
39N
36N
15W
10W
5W
0
5E
10E
15E
20E
25E
280
285
290
295
300

(b)

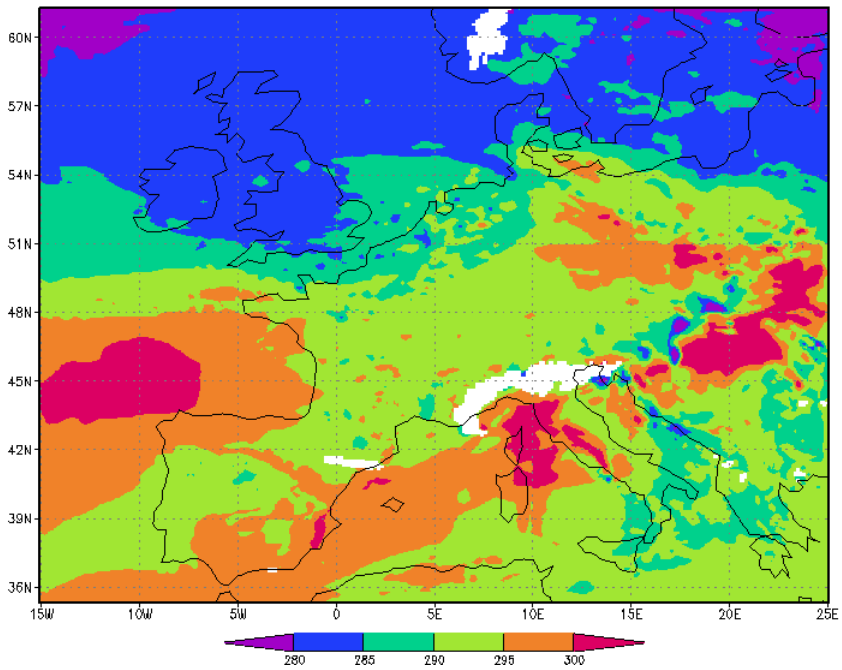
60N
57N
54N
51N
48N
45N
42N
39N
36N
15W
10W
5W
0
5E
10E
15E
20E
25E
280
285
290
295
300

(c)

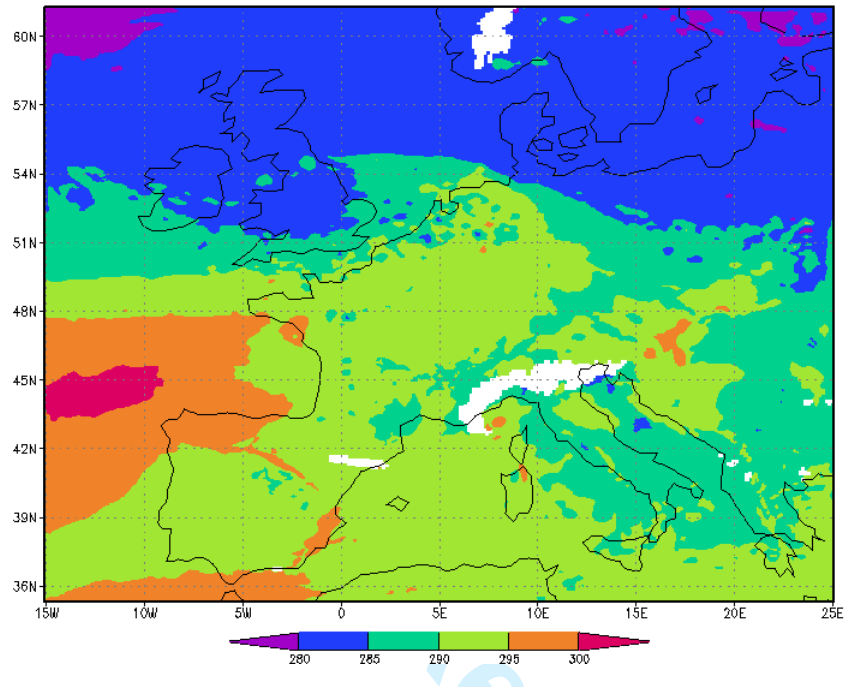
60N
57N
54N
51N
48N
45N
42N
39N
36N
15W
10W
5W
0
5E
10E
15E
20E
25E
280
285
290
295
300

(d)

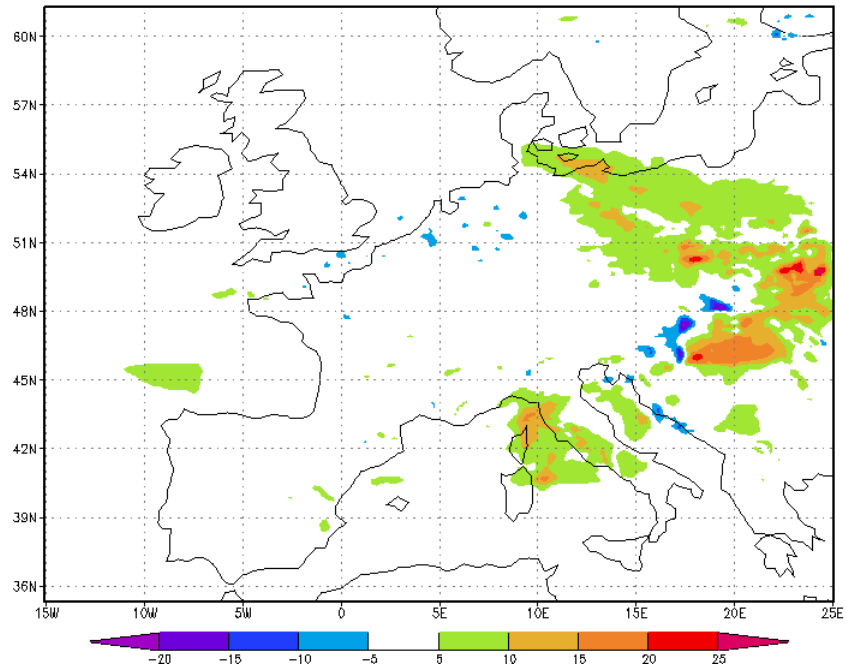
60N
57N
54N
51N
48N
45N
42N
39N
36N
15W
10W
5W
0
5E
10E
15E
20E
25E
−20
−15
−10
−5
5
10
15
20
25

(e)

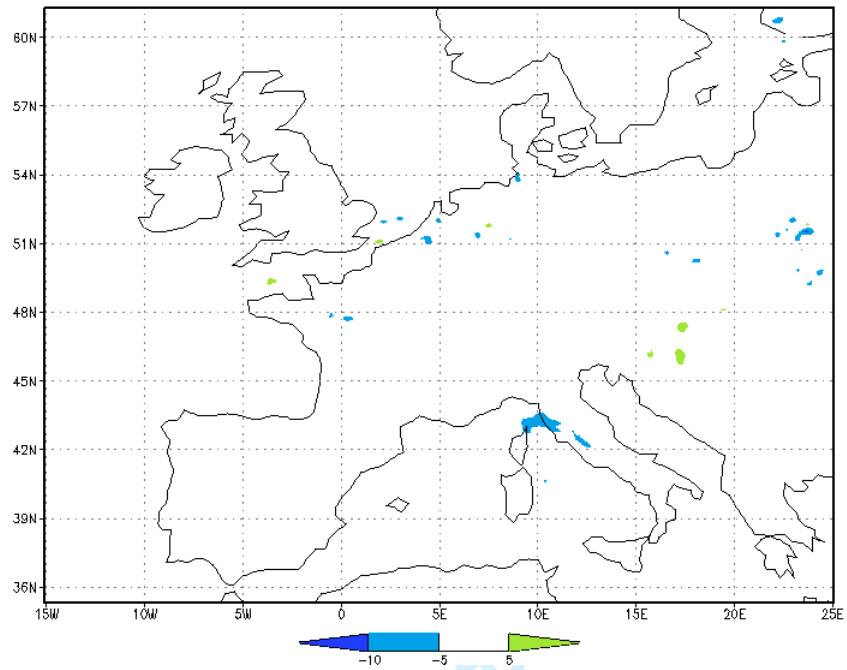

Figure 2. Potential temperature (K) at 850 hPa and the corresponding analysis increments (i.e., differences between the analysis and the first guess), obtained in the experiments without and with cloud ice adjustment. The first guess (1-h forecast) is shown in (a), the analysis without cloud ice adjustment is plotted in (b) and the analysis with cloud ice adjustment is given in (c). The corresponding analysis increments are shown in (d) and (e) for the experiments without and with cloud ice adjustment, respectively.

(a)

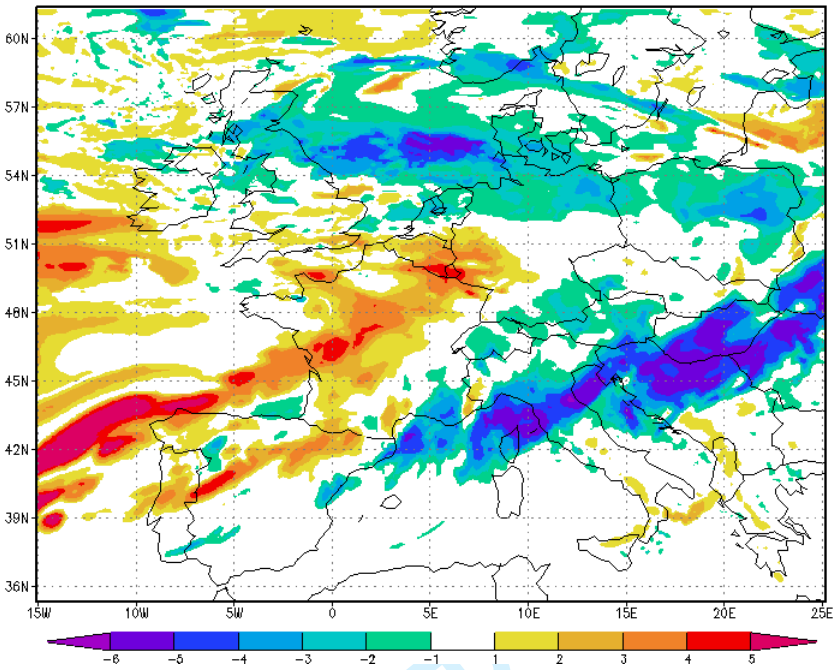
60N
57N
54N
51N
48N
45N
42N
39N
36N
15W
10W
5W
0
5E
10E
15E
20E
25E
−6
−5
−4
−3
−2
−1
1
2
3
4
5

(b)

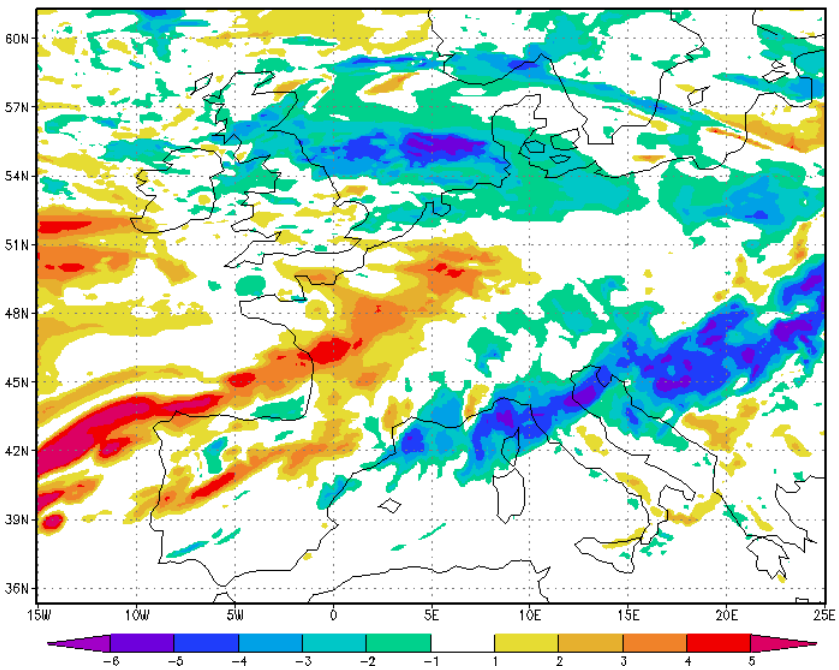
60N
57N
54N
51N
48N
45N
42N
39N
36N
15W
10W
5W
0
5E
10E
15E
20E
25E
−6
−5
−4
−3
−2
−1
1
2
3
4
5

(c)

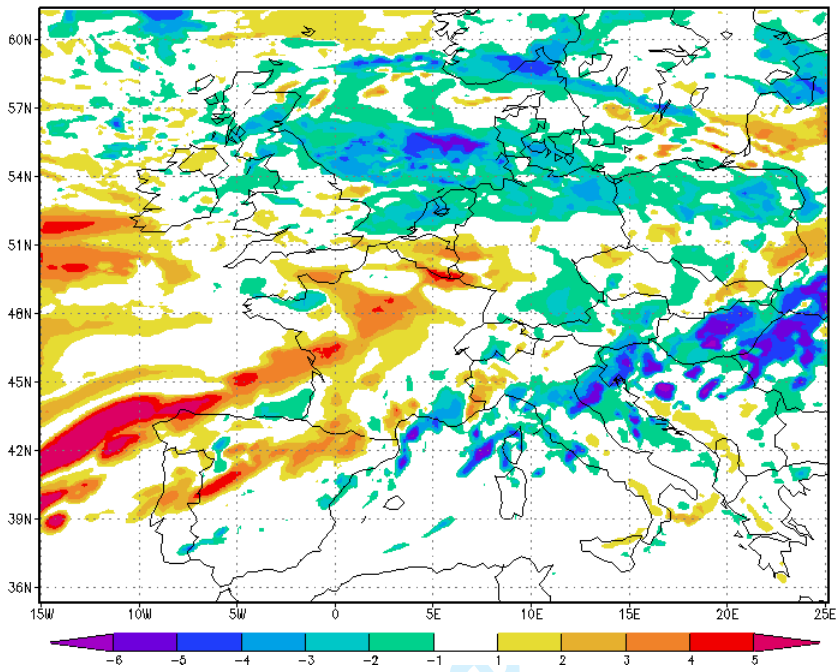

Figure 3. Differences calculated between the model-simulated and the "observed" 10.35 μm radiances for (a) the first guess forecast, (b) the analysis without cloud ice adjustment and (c) the analysis with cloud ice adjustment. The differences correspond to the end of the first data assimilation cycle (1300 UTC 18 Jan 2007). The units for radiances are W m^{-2} sr^{-1} cm.

(a)

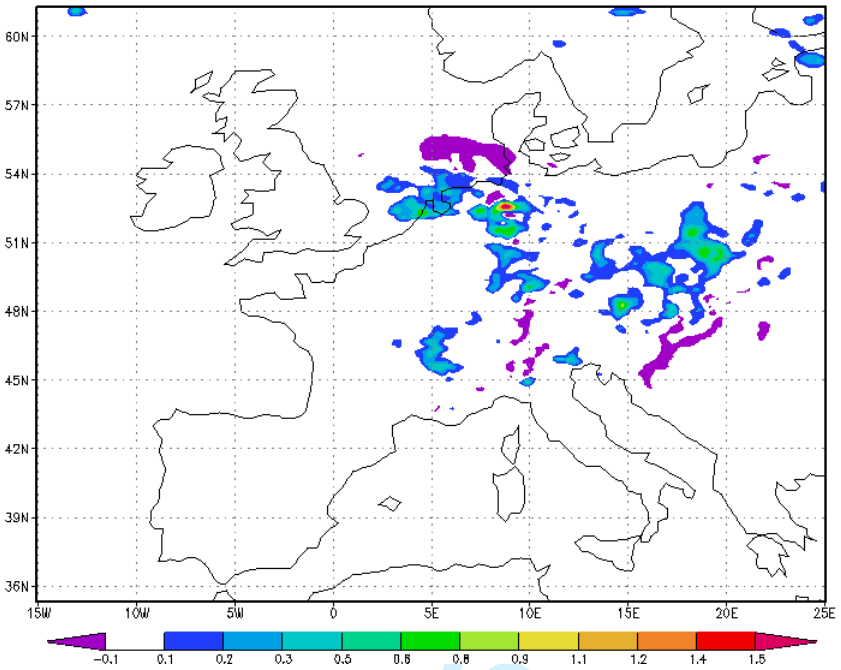
60N
57N
54N
51N
48N
45N
42N
39N
36N
15W
10W
5W
0
5E
10E
15E
20E
25E
-0.1
0.1
0.2
0.3
0.5
0.6
0.8
0.9
1.1
1.2
1.4
1.5

(b)

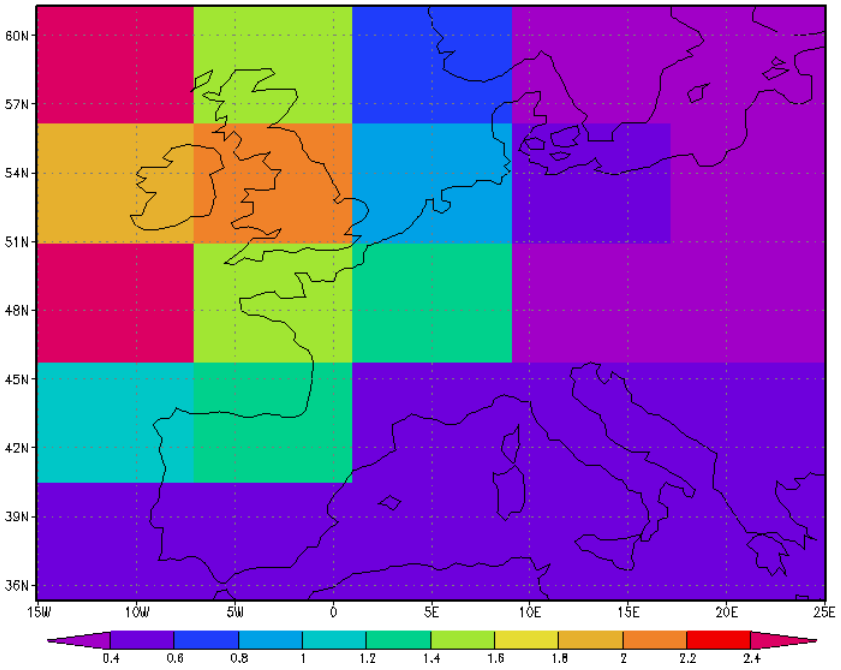
60N
57N
54N
51N
48N
45N
42N
39N
36N
15W
10W
5W
0
5E
10E
15E
20E
25E
0.4
0.6
0.8
1
1.2
1.4
1.6
1.8
2
2.2
2.4

(c)

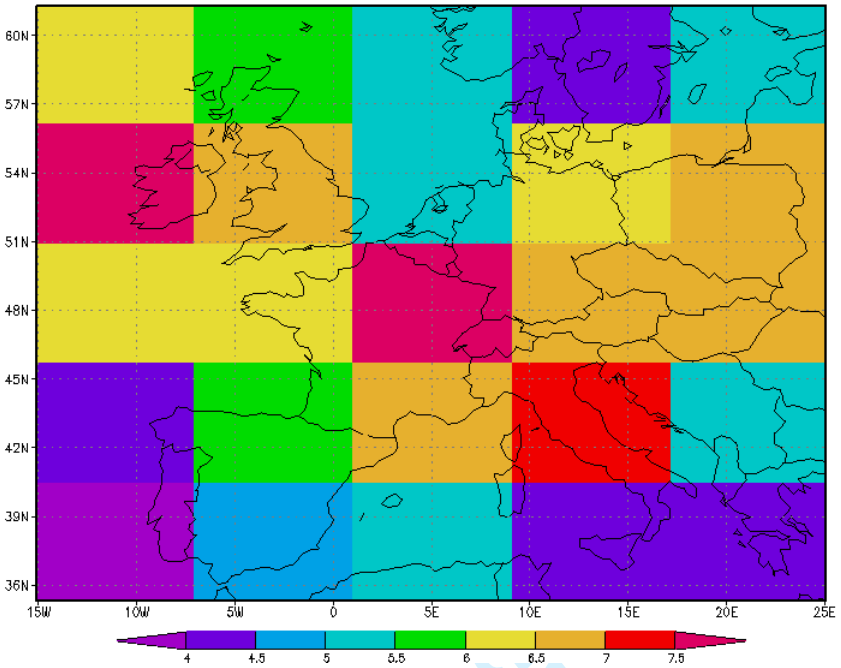

Figure 4. (a) Cloud ice analysis increments (in units of g kg^{-1}) at 600 hPa level obtained in the experiment with the cloud ice adjustment in the first data assimilation cycle (1300 UTC 18 Jan 2007). Information content of the assimilated observations (DFS, Eq. 6) calculated in the same data assimilation cycle is shown for the experiment without cloud ice adjustment in (b) and for the experiment with cloud ice adjustment in (c). The DFS in (b) and (c) are non-dimensional quantities, which count the total number of independent pieces of information per local domain (block).

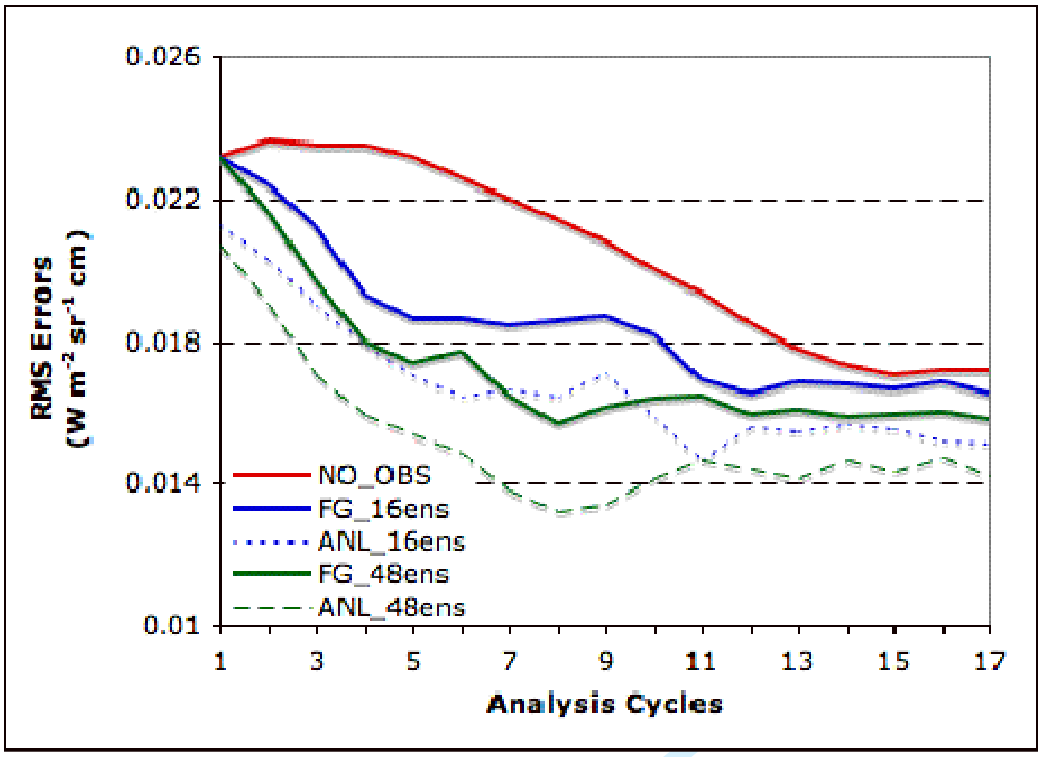

Figure 5. RMS errors of the analysis (ANL, dashed lines) and the first guess (FG, solid lines) calculated with respect to the RAMS-simulated 10.35 μm radiances and plotted as functions of data assimilation cycles. Results from the experiments with 16 and 48 ensemble members are shown. For reference, the RMS errors of the experiment without data assimilation (NO_OBS, solid line) are also included. Units for radiances are W m^{-2} sr^{-1} cm.

(a)

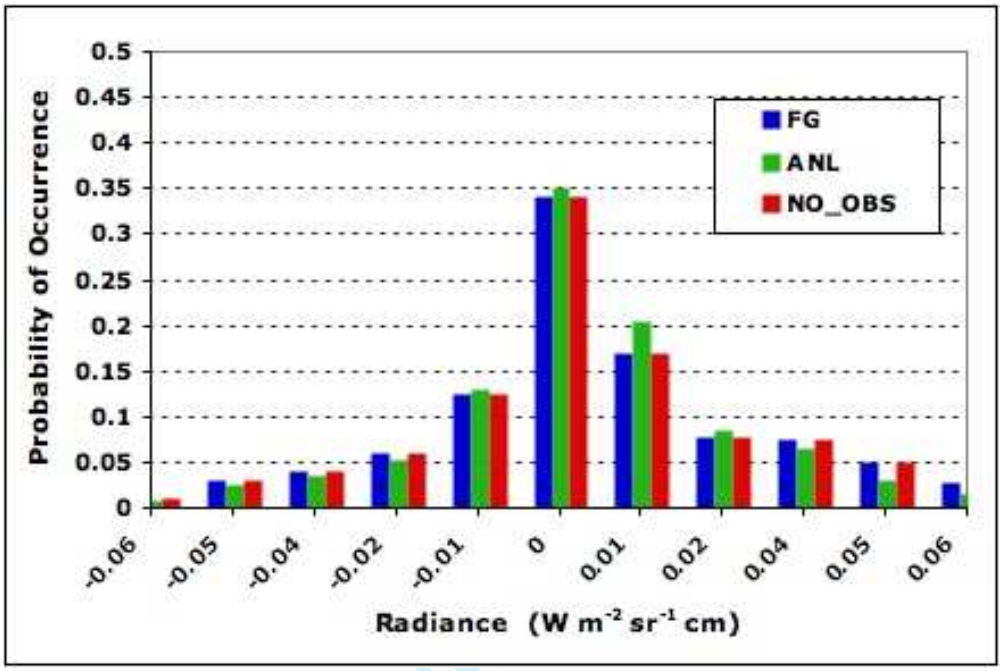

(b)

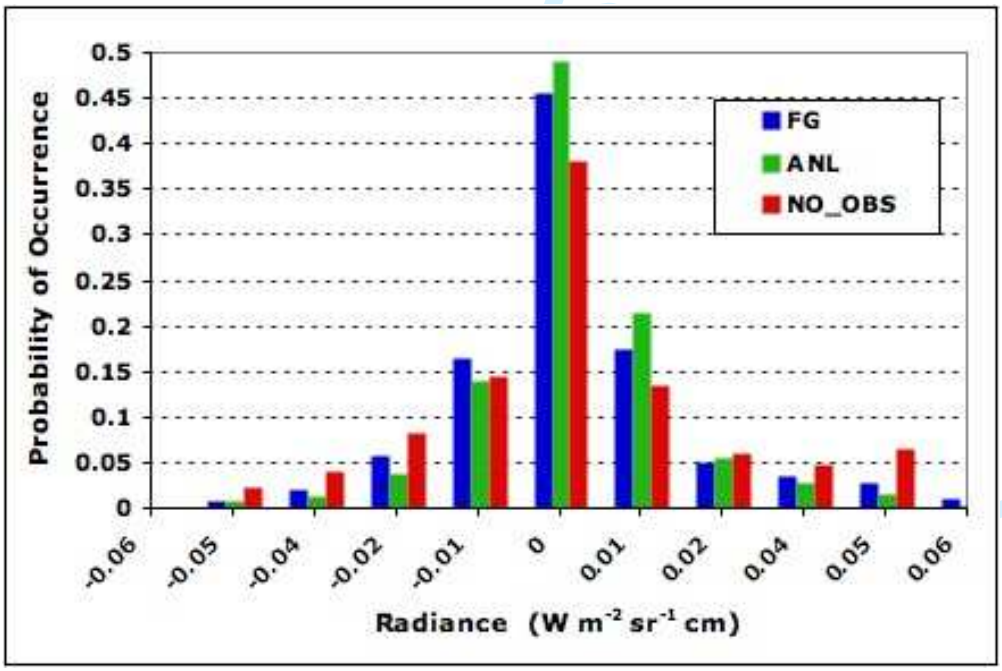

Figure 6. Probability histogram of the errors of the 10.35 μm radiances, calculated with respect to RAMS-simulated radiances, for the first guess (FG), the analysis (ANL) and the experiment without assimilation (NO_OBS). Data assimilation experiments using ensemble size of 48 members are shown. Results from first (a) and seventh (b) data assimilation cycle are presented. Units for radiances are W m^{-2} sr^{-1} cm.

(a)

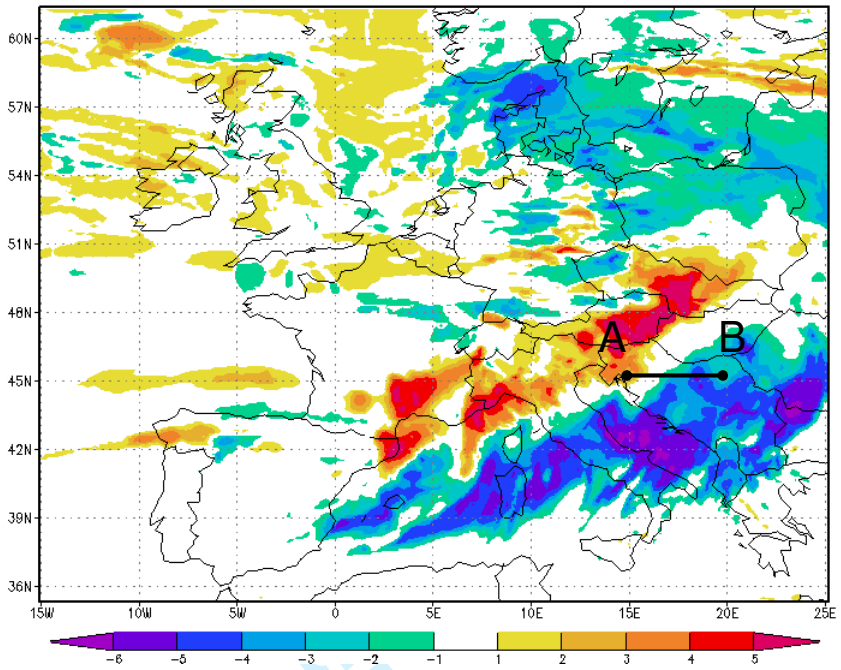
60N
57N
54N
51N
48N
45N
42N
39N
36N
15W
10W
5W
0
5E
10E
15E
20E
25E
A
B
−6
−5
−4
−3
−2
−1
1
2
3
4
5

(b)

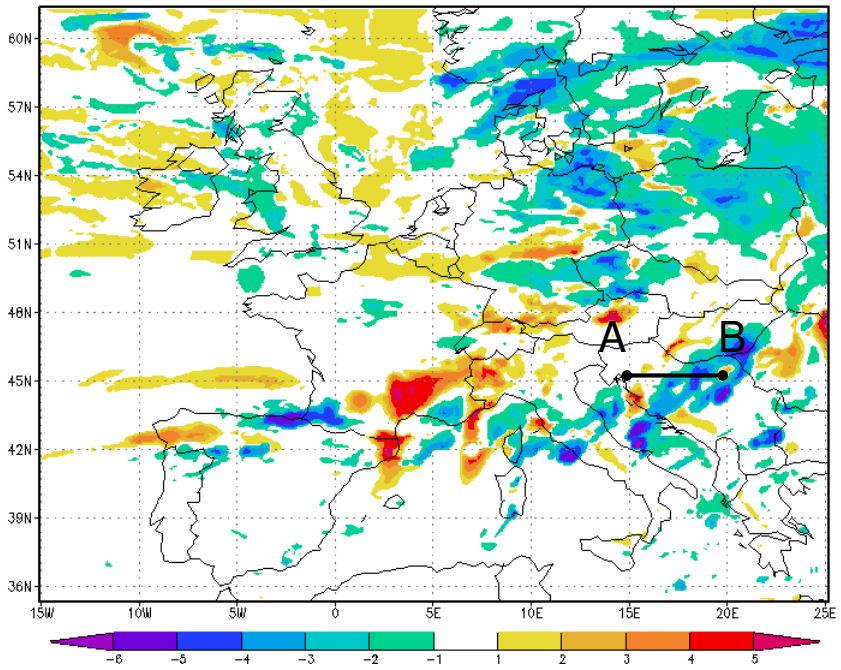
60N
57N
54N
51N
48N
45N
42N
39N
36N
15W
10W
5W
0
5E
10E
15E
20E
25E
A
B
−6
−5
−4
−3
−2
−1
1
2
3
4
5

(c)

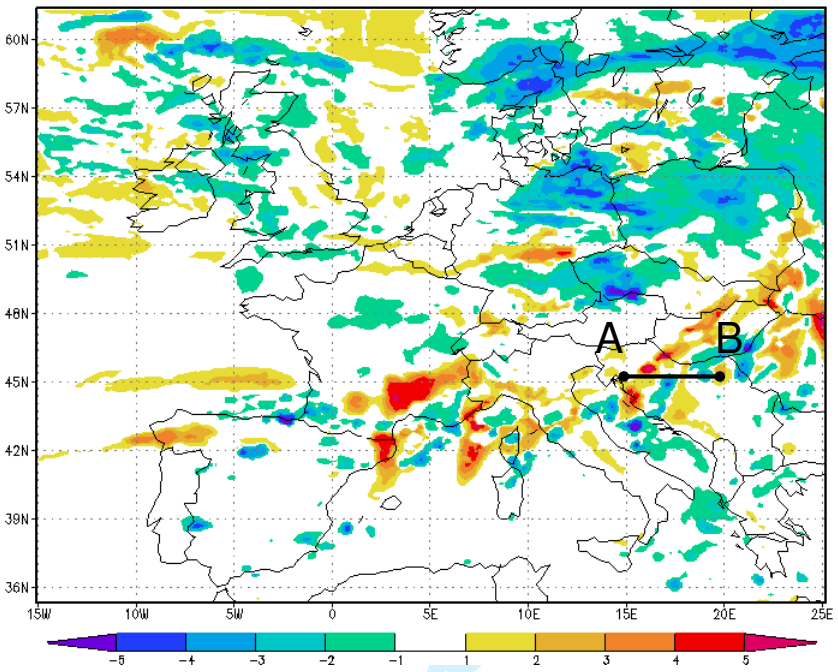

Figure 7. Differences, corresponding to the end of the seventh data assimilation cycle (1900 UTC 18 Jan 2007), calculated between the model-simulated and the "observed" 10.35 μm radiances are plotted for (a) the experiment without data assimilation (i.e., old forecast), (b) 1-h forecast used as a first guess in data assimilation, and (c) the analysis. The units for radiances are W m^{-2} sr^{-1} cm. Line AB indicates the location of the vertical cross section shown in figure 9.

(a)

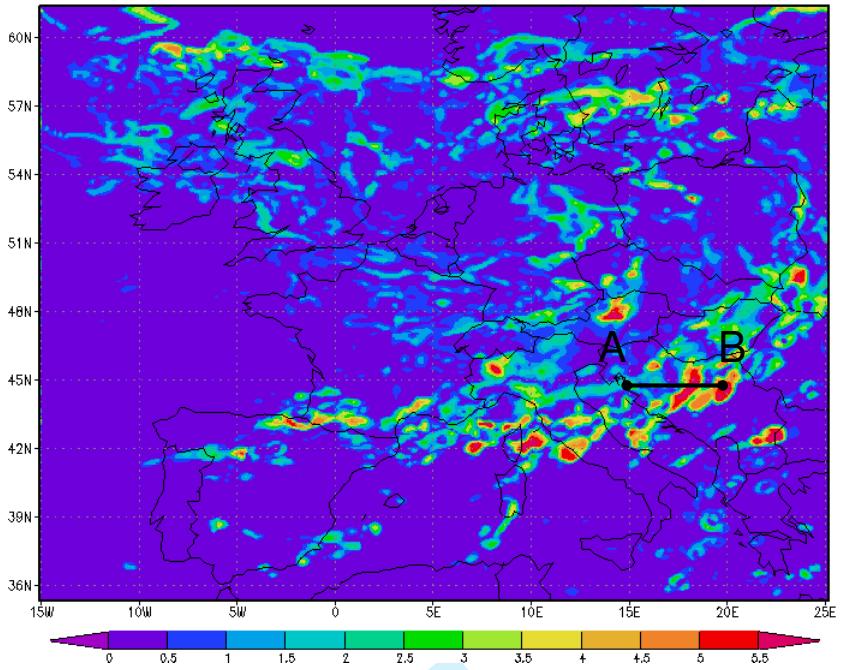

(b)

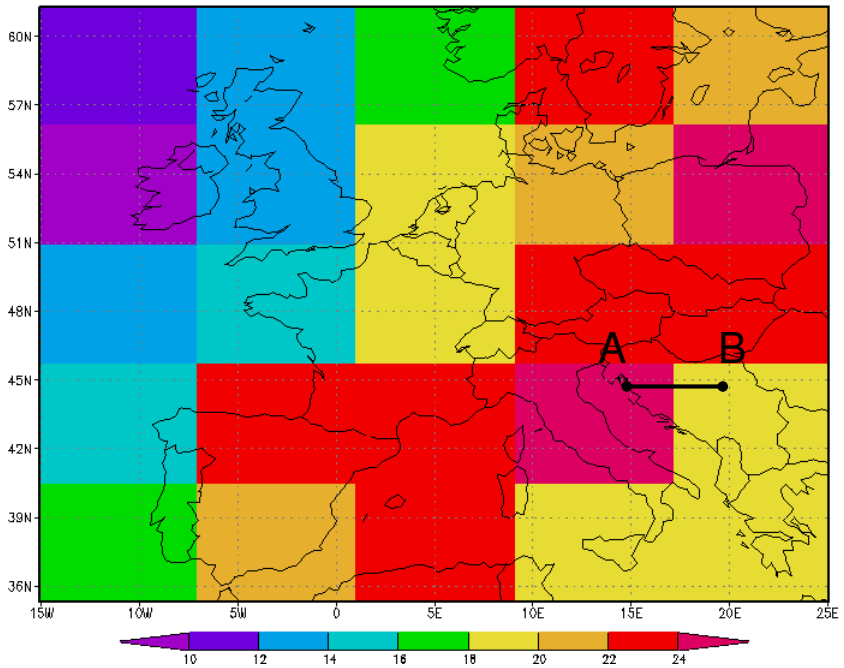

Figure 8. Analysis uncertainty for the 10.35 μm radiances (σ^{a}_{obs} , Eq. 7) is plotted in (a) and the corresponding DFS (Eq. 6) is shown in (b). The results are given for the seventh data assimilation cycle, thus are comparable to the results in figure 7. The units for radiances are W m^{-2} sr^{-1} cm, however the values are scaled by 100.

(a)

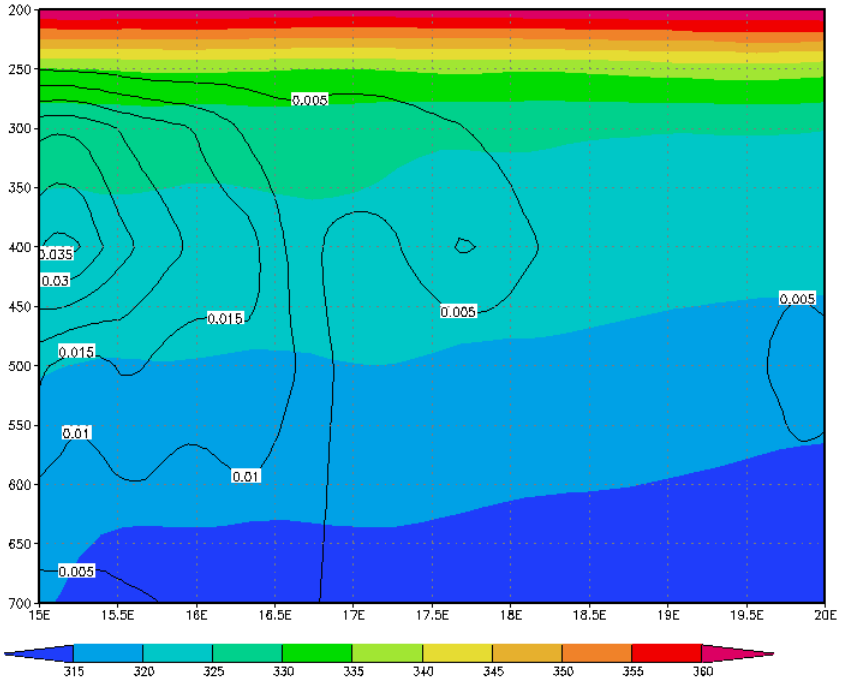
200
250
300
350
400
450
500
550
600
650
700
15E
15.5E
16E
16.5E
17E
17.5E
18E
18.5E
19E
19.5E
20E
0.005
0.035
0.03
0.015
0.005
0.005
0.015
0.01
0.01
0.005
315
320
325
330
335
340
345
350
355
360

(b)

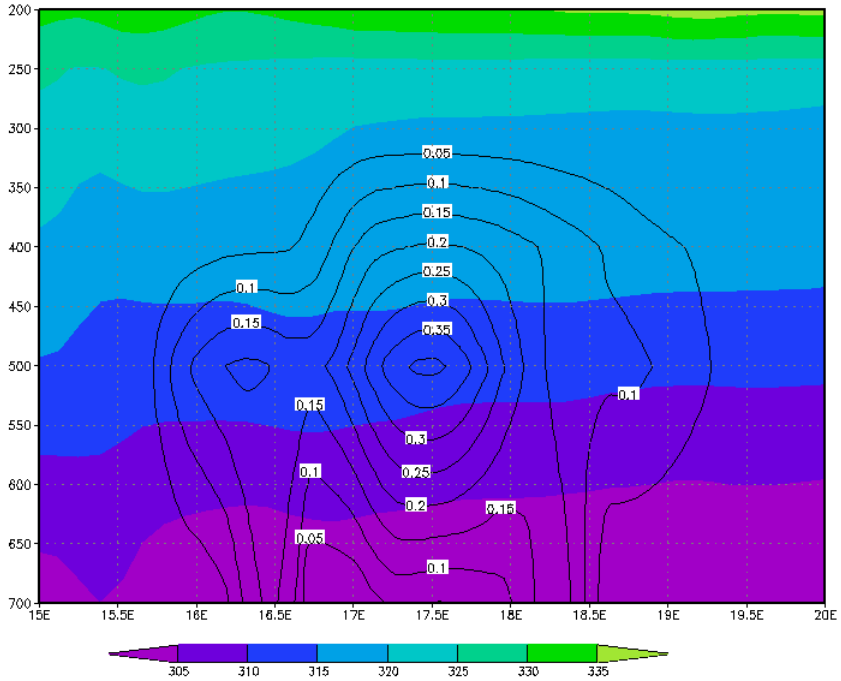
200
250
300
350
400
450
500
550
600
650
700
15E
15.5E
16E
16.5E
17E
17.5E
18E
18.5E
19E
19.5E
20E
0.05
0.1
0.15
0.2
0.25
0.3
0.35
0.1
0.15
0.15
0.1
0.3
0.1
0.25
0.2
0.15
0.05
0.1
305
310
315
320
325
330
335

(c)

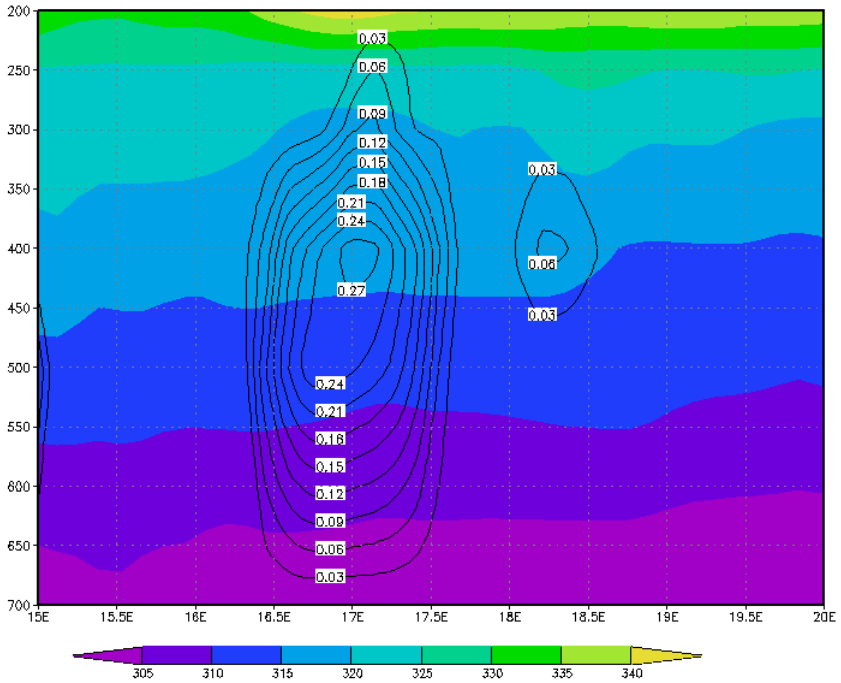

(d)

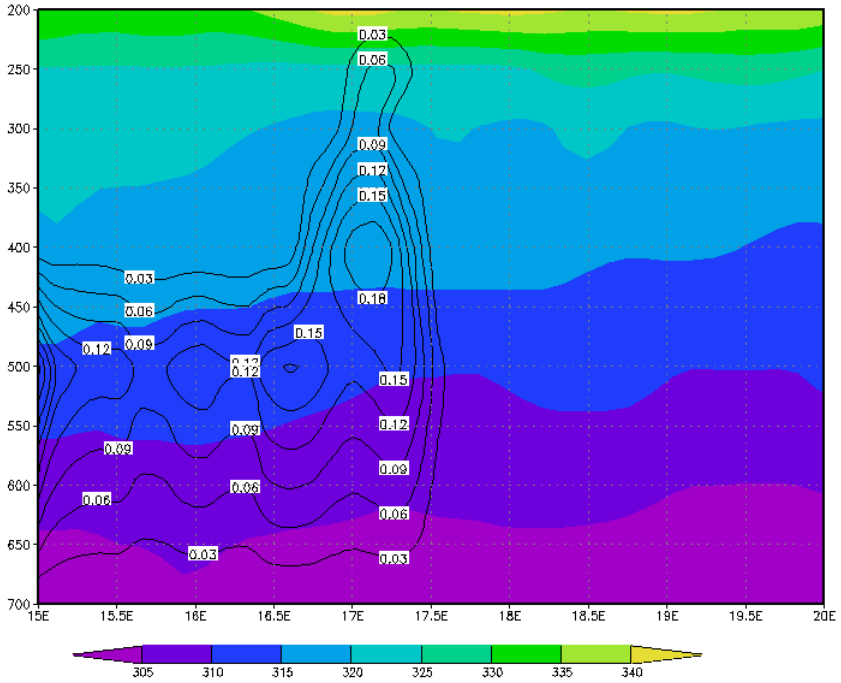

Figure 9. Vertical cross section taken along the line AB shown in figures 7 and 8. Potential temperature (shading) and cloud ice (contours) are shown in the figure. The results are valid at the end of seventh data assimilation cycle (1900 UTC 18 January 2007). The "observations" (RAMS forecasts) are given in panel (a), the forecast results from the experiment without assimilation are shown in (b), the 3-h background in (c) and the analysis in (d). Units for potential temperature are K and for cloud ice g kg^{-1}.